JOURNAL OF GEOPHYSICAL RESEARCH, VOL. 102, NO. B2, PAGES 2659–2679, FEBRUARY 10, 1997

Thermal evolution and slip history of the Renbu Zedong Thrust, southeastern Tibet

Xavier Quidelleur,[1] Marty Grove, Oscar M. Lovera, T. Mark Harrison, and An Yin

Department of Earth and Space Sciences and Institute of Geophysics and Planetary Physics
University of California, Los Angeles

F. J. Ryerson

Institute of Geophysics and Planetary Physics, Lawrence Livermore National Laboratory, Livermore, California

Abstract. Cretaceous granitoids of the Gangdese batholith, southeastern Tibet, were overthrust by upper greenschist to epidote-amphibolite facies Tethyan rocks derived from the Indian shelf along the north directed (~30° dip) Renbu Zedong Thrust (RZT). Thermochronological results obtained from a NE-SW transect near Lian Xian show evidence of thermal effects related to thrusting. Granitoids immediately beneath the RZT exhibit considerable recrystallization to greenschist facies assemblages. Biotite and K-feldspar $^{40}Ar/^{39}Ar$ ages measured along the traverse into the footwall increase systematically away from the RZT. The timing of initial upward displacement of the RZT hanging wall is constrained to have occurred at ~18 Ma from the hornblende ages and the two K-feldspar samples closest to the fault. K-feldspars up to 15 km from the thrust yield 9-12 Ma ages for the initial ~20% of ^{39}Ar release. Distal samples yield $^{40}Ar/^{39}Ar$ ages nearly as old as the 70-110 Ma ion microprobe $^{206}Pb^{*}/^{238}U$ ages determined for coexisting zircons. We have integrated our thermal history results with numerical heat flow models and found that while reheating to 320-280°C at shallow (~7 km) levels due to rapid (>15 mm/yr) slip along the RZT at ~10 Ma is capable of explaining the initial portion of the K-feldspar age spectra, a prior common thermal history experienced by all samples cannot satisfactorily account for all the $^{40}Ar/^{39}Ar$ results. Instead, we find our thermal history constraints to be more completely explained by a numerical model in which (1) rocks currently at the surface originated from different depths,(2) footwall samples in close proximity to the RZT experienced fault drag from 19 to 15 Ma and (3) post-thrusting denudation of the region involving localized tilting occurred at ~10 Ma. The minimum average slip rate and displacement along the ramp during this period are 2 mm/yr and 12 km, respectively, but are likely to have been greater. The cooling episode recorded in all the K-feldspar age spectra beginning at ~10 Ma may either reflect denudation following regional uplift due to displacement along the ramp of the Main Himalayan Thrust or topographic collapse following cessation of RZT thrusting.

Introduction

Knowing the timing and sequence of thrusting within the Himalaya and southern Tibet is pivotal to understanding the evolution of this unique mountain system. It has long been suspected [*Gansser*, 1964] that thrusting within the Himalaya is a relatively late response, forestalled for perhaps 20-30 m.y. [*Harrison et al.*, 1992; *Yin et al.*, 1994] following the onset of India's collision with Asia, which began at about 50 Ma [e.g., *Burbank et al.*, 1996]. The south directed crustal-scale thrusts within the Himalaya, including the Main Central Thrust (MCT), Main Boundary Thrust (MBT), and the Main Frontal Thrust (MFT) [*Gansser*, 1964; *LeFort*, 1975; *Bouchez and Pêcher*, 1981; *Mattauer*, 1986; *Burbank et al.*, 1996] all appear to sole into a common decollement, termed the Main Himalayan Thrust (MHT) by *Zhao et al.* [1993]. In general, the MCT places high-grade Indian gneisses atop medium-grade schists, the MBT juxtaposes those schists against unmetamorphosed Miocene molasse, and the MFT is presently active. Farther north, within the Tethyan Himalaya, south directed thrust imbricates generally juxtapose greenschist grade rocks suggesting relatively small displacements [*Wang et al.*, 1983; *Burg*, 1983; *Burg et al.*, 1984; *Yin et al.*, 1994]. North of the Indus-Tsangpo suture, the south directed, Gangdese Thrust (GT) has placed Late Cretaceous-Early Tertiary granitoids representing a precollisional magmatic arc (the Gangdese batholith) of Asian affinity over both Late Cretaceous-Early Tertiary forearc strata and a collisional melange including ophiolite and related suture zone assemblages [*Yin et al.*, 1994]. Zircon U-Pb results and $^{40}Ar/^{39}Ar$ thermochronology indicate that the GT was active during the late Oligocene-early Miocene [*Yin et al.*, 1994; T.M. Harrison, unpublished data 1996].

[1]Now at Institut de Physique du Globe de Paris, Université Paris Sud, France.

Copyright 1997 by the American Geophysical Union.

Paper number 96JD02483.
0148-0227/97/96JD-02483$09.00

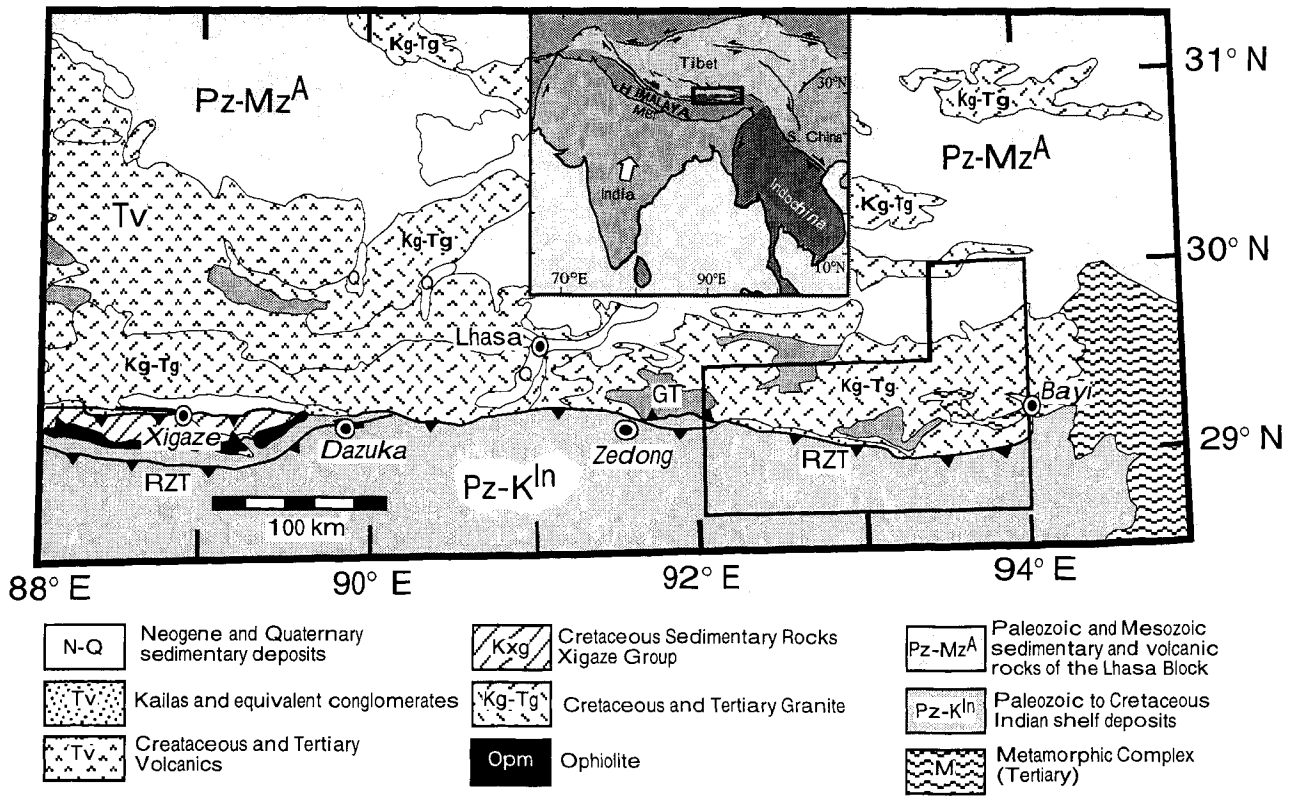

Figure 1. The geological map shows the location of the Indus-Tsangpo suture zone which separates the Lhasa block from Indian shelf assemblages. In southeastern Tibet, the suture zone is dominantly marked by the Renbu Zedong Thrust (RZT). The Lhasa block is characterized by Paleozoic to Mesozoic sedimentary and volcanic rocks intruded by Cretaceous to Tertiary granitoid rocks of the Gangdese batholith. The location of Figure 2 is shown by the polygon. Inset is generalized tectonic map of Asia showing major crustal-scale faults (MBT, Main Boundary Thrust) and indicating the location of the geological map.

The relatively late discovery of the south directed GT is due to the fact that a younger, north directed thrust, termed the Renbu Zedong Thrust (RZT), generally obscures its exposure [*Yin et al.*, 1994].

The RZT truncates the GT, burying both the GT and its hanging wall granitoids beneath the RZT hanging wall, which consists of predominately low-grade Tethyan shelf rocks derived from the northern margin of India (Figure 1). The RZT was first mapped by Chinese geologists [*Wang et al.*, 1983] and later appeared locally on regional compilations of southern Tibetan geology [*Burg*, 1983; *Liu et al.*, 1988; *Kidd et al.*, 1988]. Our own field work has consolidated these observations and confirms that with the exception of the Zedong window (Figure 1), the RZT defines the "suture" between rocks of Indian and Asian affinities from Renbu to the eastern syntaxis (Figure 1). Both regional geologic relationships and mesoscopic structures including asymmetric folds and thrusts directly above the RZT confirm that the thrust is north directed. South dipping cleavage and north verging isoclinal folds in the Tethyan metasediments immediately above the fault also indicate northward thrusting along the RZT [*Yin et al.*, 1994].

Although the RZT is the dominant structural feature along the suture zone in southern Tibet [*Wang et al.*, 1983; *Burg*, 1983; *Liu et al.*, 1988; *Kidd et al.*, 1988; *Yin et al.*, 1994], its timing and kinematics have not previously been well studied. The RZT is clearly younger than the GT as its hanging wall strata are locally thrust over the trace of the GT, putting both the hanging wall and footwall rocks of the GT in the RZT footwall. This relationship thus places an upper age limit on the RZT of ~23 Ma [*Yin et al.*, 1994]. Because the RZT appears not to be offset by the north-south trending Yadong-Gulu rift, dated at 8±1 Ma [*Harrison et al.*, 1995a], we infer that its activity is restricted to the interval 23 to 8 Ma. A possible indication of the time of displacement along the RZT was obtained from a K-Ar age of white mica filling a synkinematic tension gash in the RZT shear zone near Dazuka (Figure 1) [*Ratschbacher et al.*, 1994]. The 17.5±0.9 Ma age potentially dates mica growth during low-grade metamorphism.

Reheating of the footwall beneath a major overthrust potentially allows the slip history of the fault to be estimated through the combined use thermochronology and numerical heat flow models. Numerical heat flow calculations indicate that relatively high displacements rates (>15 mm/yr) are required to bring about significant temperature increase (>100°C) within a stationary footwall beneath a major overthrust. This estimate also depends upon associated effects, such as shear heating, fluid circulation within the fault zone, and topographic effects. In this paper, we present $^{40}Ar/^{39}Ar$ thermal history results from granitoid samples collected in a traverse from the trace of the RZT into its footwall. In addi-

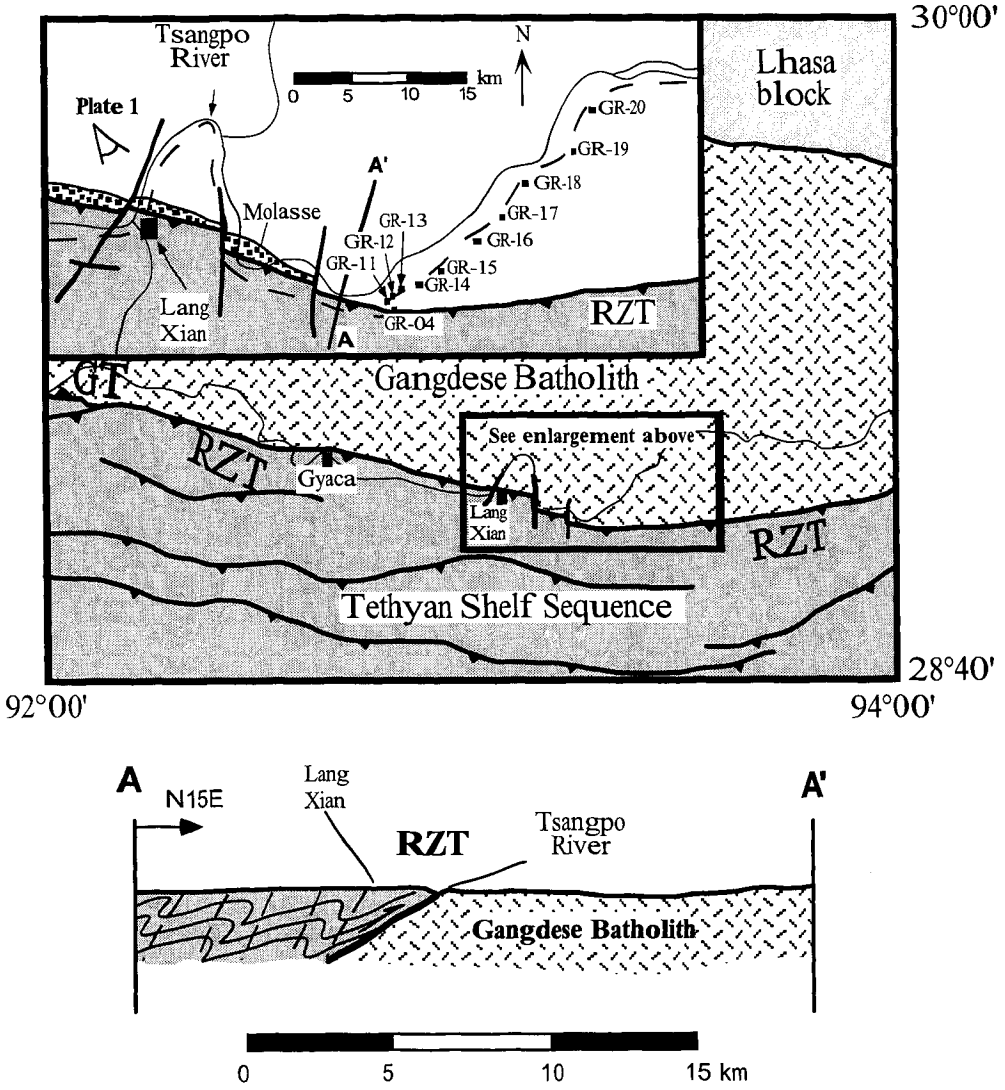

Figure 2. Sketch map of the study area showing the relationship between the Renbu-Zedong Thrust (RZT) and the Gangdese batholith. Inset shows locations of granitoid samples sampled from the footwall. The schematic cross section shows the orientation of the RZT. Location of Plate 1 is indicated.

tion, we report ^{238}U-^{206}Pb zircon ages which constrain the timing of prior pluton emplacement. These results show clear evidence of a thermal imprint that we relate to thrusting and permit us to evaluate models describing the RZT slip history. This analysis has led us to conclude that the RZT was active between 19 and 10 Ma. Although the RZT is out-of-sequence thrust with respect to the GT and the Himalayan thrusts, this estimate of its timing fills an otherwise unrepresented interval in the Oligo-Miocene history of thrusting in the Himalaya and southern Tibet.

Geologic Setting

Between Renbu and the Zedong window (Figure 1, inset), the nature of the RZT is obscured due to both structural complexity (e.g., thrust imbricates) and burial beneath the wide Tsangpo river channel deposits. East of the Zedong window, however, the geological relationships are straightforward and the RZT is well exposed. During fieldwork in 1994, we encountered geological relationships that permitted us to systematically sample the granitoids within the footwall of the RZT at progressively greater distances from the fault. Near Lang Xian (Figure 2), the Tsangpo river turns abruptly north providing excellent exposure of the RZT (Plate 1). Here, the fault places Tethyan phyllites directly atop a ~100-m-thick section of deformed Kailas-type molasse [*Harrison et al.*, 1993] which is itself deposited nonconformably on granitoids of the Gangdese batholith (Figure 2, inset). Farther east, the Tsangpo turns northeast into the footwall of the RZT (Figure 2a). Here we collected 12 granitoid samples from exposures along the Tsangpo river. Our 25-km sampling traverse along the river valley occurs along a trend that diverges at ~40° from the surface trace of the RZT (Figure 2, inset and Table 1). Assuming a constant 30° dip to the south for the fault (Plate 1), our samples are situated between 0 and 9 km beneath the RZT.

At the beginning of the traverse, the faulted contact between the metasediments and Gangdese batholith granitoids is clearly exposed with intrusive rock below the RZT penetratively deformed and recrystallized to greenschist facies.

Plate 1. Photo taken toward the southeast immediately north of Lang Xian (see Figure 2 for exact location) showing the thrust contact between the Tethyan metasediments in the hanging wall and sheared materials of the Gangdese batholith in the footwall.

Table 1. Samples Locations and $^{40}Ar/^{39}Ar$ Biotite and K-Feldspar Ages

Sample	Horizontal Distance From RZT, km	Biotite Total Fusion Age[a] ±1σ, Ma	K-feldspar Total Gas Age[b] Ma	Calculated $\%K_2O$ in K-feldspar[c]
GR-04	0.0	12.3±0.2	12.8	14.4
GR-10	0.3	-	-	-
GR-11	0.6	14.9±0.8	14.5	12.2
GR-12	0.8	25.1±0.8	22.0	12.3
GR-13	1.6	34.1±4.6	17.6	15.4
GR-14	2.4	35.7±1.7	20.8	15.5
GR-15	3.8	51.6±3.8	31.6	16.0
GR-16	7.0	63.6±1.8	39.3	17.1
GR-17	9.0	58.2±1.4	-	-
GR-18	11.7	61.4±0.9	33.0	16.1
GR-19	15.2	58.5±0.9	24.0	15.9
GR-20	18.2	42.5±0.3	24.8	15.2

[a]Weighted mean of five replicate analyses.
[b]Calculated from step-heating age results weighted by ^{39}Ar release.
[c]Calculated from sample weight, J factor, and total ^{39}Ar yield.

Close to the RZT, recrystallization in the footwall includes replacement of biotite by chlorite±prenhite±sphene, reaction of amphibole to chlorite+epidote, and alteration of plagioclase to albite+quartz+epidote±calcite. This greenschist facies alteration abruptly decreases in intensity over a distance of 1 km and is imperceptible at ~5 km from the RZT. The spatial association of retrograde overprinting to the RZT in the footwall implies that mild heating and/or access to fluids occurred in response to overthrusting of the Tethyan metasediments.

Rocks within the hanging wall are characterized by perceptibly higher grade (upper greenschist to lower amphibolite facies) metamorphism than is typically found in the Tethyan metasediments farther west [e.g., *Ratschbacher et al.*, 1994; *Yin et al.*, 1994]. Directly above the RZT for example, biotite-grade schists are exposed and locally derived float blocks contain garnet-bearing, epidote amphibolite mafic schist are present. Existence of these assemblages indicates that temperatures at the base of the hanging wall were potentially as high as ~450°C at the time of thrusting.

Results

Below we present $^{40}Ar/^{39}Ar$ (biotite and K-feldspar) and ion microprobe $^{206}Pb/^{238}U$ (zircon) analysis of materials sampled as a function of distance from the surface trace of the RZT. Interpretation of $^{40}Ar/^{39}Ar$ thermochronologic results from granitic rocks in the footwall is facilitated by knowledge of their emplacement ages. In addition, $^{40}Ar/^{39}Ar$ analyses obtained from hornblendes obtained from the hanging wall immediately adjacent to the RZT provide high-temperature thermochronologic constraints for the base of the upper plate. Details of the analytical approaches employed are outlined in Appendixes A and B, respectively. Thermal history modeling of the $^{40}Ar/^{39}Ar$ K-feldspar results is then described. Additional details appear in Appendix C. Finally, numerical heat flow calculations performed to evaluate the thermochronologic results in terms of the slip history of the RZT are discussed.

RZT Hanging Wall

Hornblendes extracted from hanging wall garnet-bearing epidote amphibolite facies mafic schists near the RZT yield isochron ages of 17.9±0.4 Ma and 17.6±0.4 Ma (Figure 3). We interpret these ages as approximating the time that the presently exposed hanging wall had cooled below ~ 450-550°C [*Baldwin et al.*, 1990]. Inasmuch as the peak temperature of recrystallization recorded by metamorphic mineral assemblages within these rocks indicate that they are unlikely to have exceeded ~ 450-550°C, we regard it likely that the hornblende ages record the time of initial motion of the RZT hanging wall toward the surface due to slip along the thrust.

RZT Footwall

U-Pb zircon ages. Single-grain, $^{206}Pb/^{238}U$ apparent ages calculated from ion microprobe analyses of granitoids from the footwall are dominantly Late Cretaceous (Table 2 and Figure 4). Because of the low radiogenic ^{207}Pb levels (~50%) of these relatively young, U-poor zircons, there is a large uncertainty associated with the calculation of $^{207}Pb/^{235}U$ ages limiting our ability to assess the concordance of the U-Pb system in these materials. We evaluated crystallization ages by plotting the $^{206}Pb/^{238}U$ and $^{207}Pb/^{235}U$ ratios uncorrected for common Pb on a concordia plot. This generally yields an array with a slope which corresponds to the common $^{207}Pb/^{206}Pb$ ratio (~1.1) and an intersection that is indistinguishable from the corrected $^{206}Pb^*/^{238}U$ age. This indicates that the U-Pb ages are concordant and that the $Pb^*/^{238}U$ ages date the time of crystallization. With the exception of a few restitic grains yielding Early Cretaceous or older ages, the majority of samples including those in close proximity to the RZT yield $^{206}Pb^*/^{238}U$ ages between 80 and 100 Ma (Table 2). From these results we conclude that (1) the emplacement ages of rocks we have examined from the RZT footwall overlap with the time of large-scale granitoid intrusion that formed the Gangdese batholith [*Allègre et al.*, 1984; *Schärer et al.*, 1984] and (2) the materials examined are derived from multiple intrusions all of which are Pre-Tertiary in age. GR-13 and GR-15 appear to be somewhat older (Late Early Cretaceous) while the youngest (GR-20) is latest Cretaceous.

Table 2. $^{206}Pb^*/^{238}U$ Ion Microprobe Zircon Results

Sample	$^{206}Pb^*/^{238}U$ Age[a], Ma ±1 S.E.	MSWD[b]	Data Points Used	Data Points Excluded From Mean
GR-04	86±2	1.0	10	
GR-10	86±1	1.2	8	120±3, 134±2
GR-11	89±11	0.4	4	358±69
GR-12	77±17	0.5	4	131±16, 129±32
GR-13	101±1	1.9	5	
GR-14	90±7	0.7	6	
GR-15	108±9	0.8	7	
GR-16	82±1	2.0	9	
GR-17	83±1	1.1	7	241±4
GR-18	84±3	-	1	136±5, 385±13
GR-19	96±3	1.1	5	234±134
GR-20	68±4	1.5	7	126±32

[a]Weighted mean age
[b]Mean Square Weighted Deviate

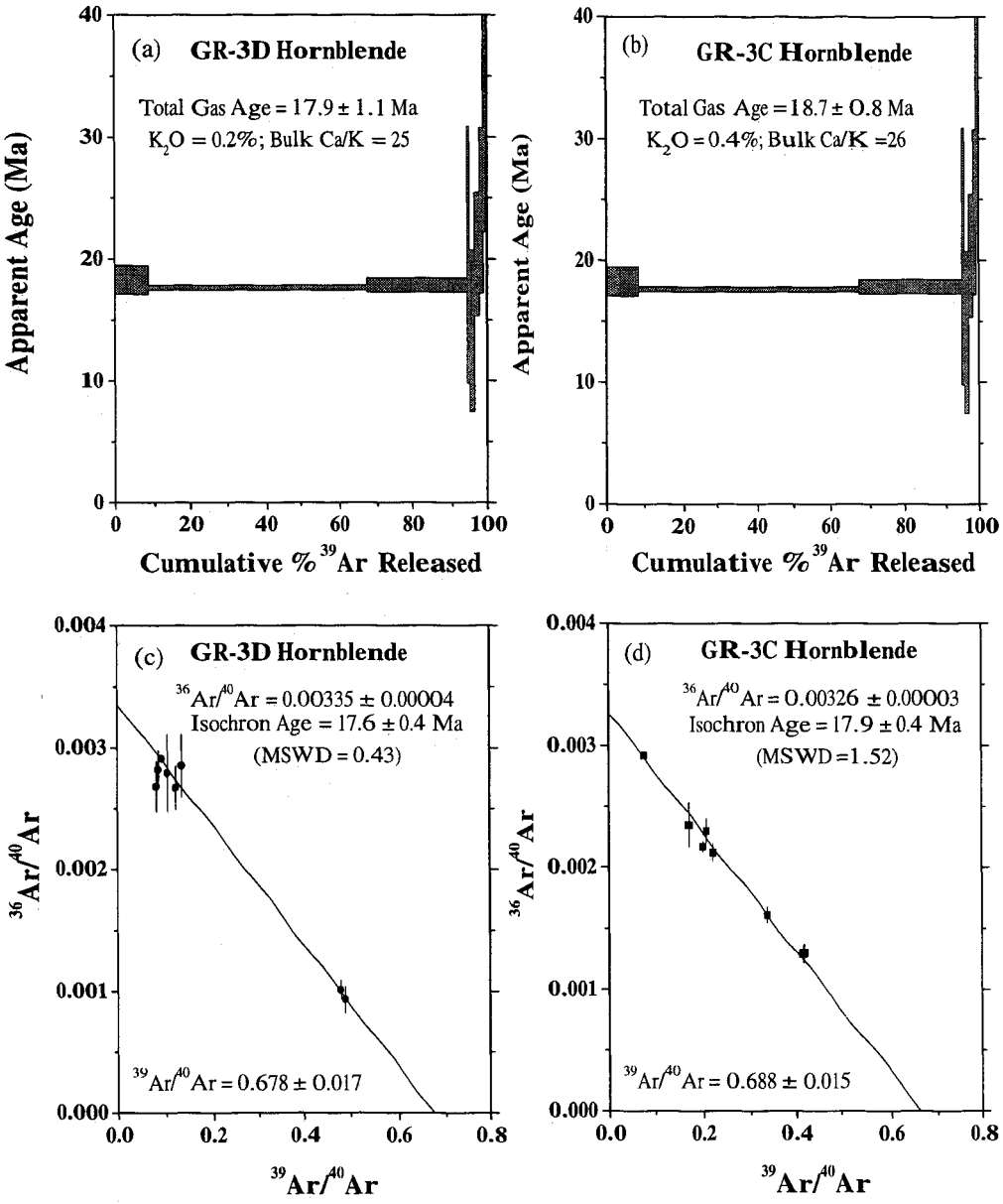

Figure 3. Hornblende $^{40}Ar/^{39}Ar$ results from garnet-bearing, epidote amphibolite mafic rocks from the hanging wall: Apparent age spectra of (a) GR-3D hornblende (b) GR-3C hornblende and $^{36}Ar/^{40}Ar$ - $^{39}Ar/^{40}Ar$ isochron of (c) GR-3D hornblende and (d) GR-3C hornblende.

Biotite and K-feldspar $^{40}Ar/^{39}Ar$ ages. Biotite was dated using the laser fusion $^{40}Ar/^{39}Ar$ method. Total fusion ages for biotite are provided in Table 1 and plotted as a function of distance from the RZT in Figure 4. Apparent ages increase regularly from 12.3 Ma at the RZT to ~60 Ma at horizontal distances greater than 5 km from the fault (2.5 km beneath the fault assuming a constant 30° dip). At distances greater than 5 km, biotite ages remain fairly constant (GR-20 is an exception). The maximum biotite ages are ~5-10 younger than the youngest $^{206}Pb/^{238}U$ zircon age (GR-20) and typically more than 20 Ma younger than the $^{206}Pb/^{238}U$ ages of the zircons with which they coexist. This disparity in apparent age for samples more than 5 km from the RZT (excluding GR-20) likely reflects protracted Ar loss due to elevated geothermal gradients and/or episodic Ar loss due to multiple intrusion during emplacement of the Gangdese batholith.

K-feldspar $^{40}Ar/^{39}Ar$ ages also increase away from the fault (Table 1). Age spectra for each of our K-feldspar samples are presented in Figure 5. Each sample was analyzed using a step-heating procedure involving isothermal duplicates for the initial heating steps. This procedure allows us to correct K-feldspar $^{40}Ar^*/^{39}Ar_K$ ratios for Cl-correlated excess radiogenic argon ($^{40}Ar^*$) derived from decrepitation of fluid inclusions [*Harrison et al.*, 1994]. Most samples (GR-04, GR-11, GR-13, GR-14, GR-15, and GR-18) yielded correlated relationships between ΔCl/K and $\Delta^{40}Ar/^{39}Ar$ determined for successive isothermal steps that permitted age corrections to be performed. After correction, the ages obtained for the initial gas released from all samples (0-20% cumulative ^{39}Ar released) was found to range from 8 to 15 Ma. Although maximum ages in the age spectra generally increased as a function of distance from the fault, the relationship is complicated by

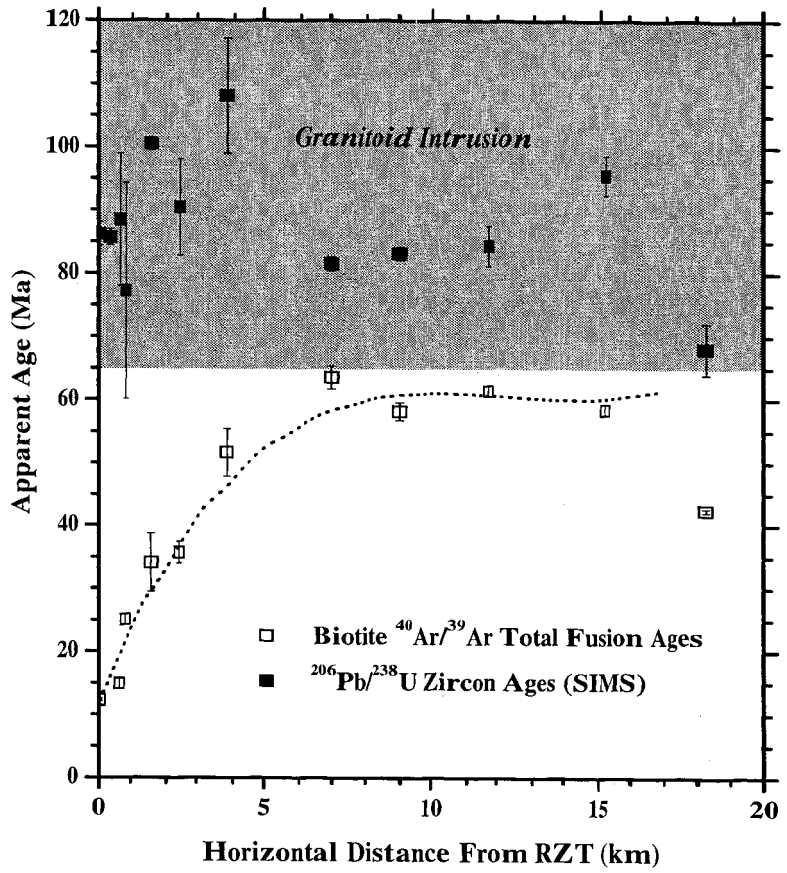

Figure 4. (top) Zircon $^{206}Pb/^{238}U$ ages as a function of horizontal distance from the trace of the RZT. Solid symbols and error bars represent weighted mean ages and standard errors. Open symbols represent measured $^{206}Pb/^{238}U$ ages of older grains not included in the calculation of the mean ages which we interpret as restite; (bottom) Biotite total-gas $^{40}Ar/^{39}Ar$ ages as a function of the horizontal distance from the RZT trace. The shaded area represents the age of intrusion of the batholith based upon the U-Pb zircon results shown above.

younger ages obtained for the most northerly samples(Figure 5i and 5j). The younger maximum ages of the GR-19 and GR-20 K-feldspar age spectra may reflect thermal effects associated with an unrelated process. GR-20 is dissimilar from the other samples in having a concave upward age spectrum that is inconsistent with an episodic loss history.

Thermal History Constraints From Biotite

The systematic increase in biotite $^{40}Ar/^{39}Ar$ fusion ages away from the trace of the RZT suggests a strong genetic link with the fault. Potentially, the data can be used to constrain the magnitude of a reheating event produced by motion of the RZT hanging wall. In Figure 6a for instance, the relationship between apparent age and the peak temperature of a 10 Ma reheating event experienced by an isobaric array of biotites that crystallized at 80 Ma and resided at ~9 km depth (250°C assuming a geothermal gradient of 25°C/km) has been calculated using Ar diffusion data for biotite and an effective diffusive length scale of 150 μm [*Harrison et al.*, 1985; *Grove and Harrison*, 1996; *Wright et al.*, 1991]. The relationship between peak temperature and distance from the RZT using the measured ages, locations of the biotite samples, and results of the diffusion calculations is shown in Figure 6c. As indicated, the distribution of biotite ages can be explained by a temperature pulse at 10 Ma that decreases exponentially from 130°C above ambient (250°C) at the fault to 60°C above ambient 15 km from the RZT. However, other models not involving reheating are also capable of reproducing the observed distribution of biotite ages and shows more compatibility with the ages obtained from the largest domains of the K-feldspars. For example, the relationship between age and ambient temperature for biotites that resided isobarically at different depths from 80 Ma until they were transported towards the surface beginning at 10 Ma is shown in Figure 6b. Assuming a geothermal gradient of 25°C/km, the observed age distribution is reproduced if sample depth from increases from 9.5 km to 11.5 km approaching the RZT (7d). Potentially deeper levels could have been exposed adjacent to the RZT by upward directed shearing of the footwall that resulted from overthrusting of the Tethyan metasediments.

K-Feldspar Thermal History Modeling

In order to recover thermal histories from the RZT footwall with the resolution to distinguish between equivalent models, the K-feldspar $^{40}Ar/^{39}Ar$ data were interpreted using the multiple diffusion domain (MDD) theory [*Lovera et al.*, 1989]. Argon diffusion studies combined with inferences from microstructural studies [*Foland*, 1974; *Harrison and McDougall*, 1982; *Zeitler*, 1987] have long indicated that low-temperature alkali feldspars are characterized by internally

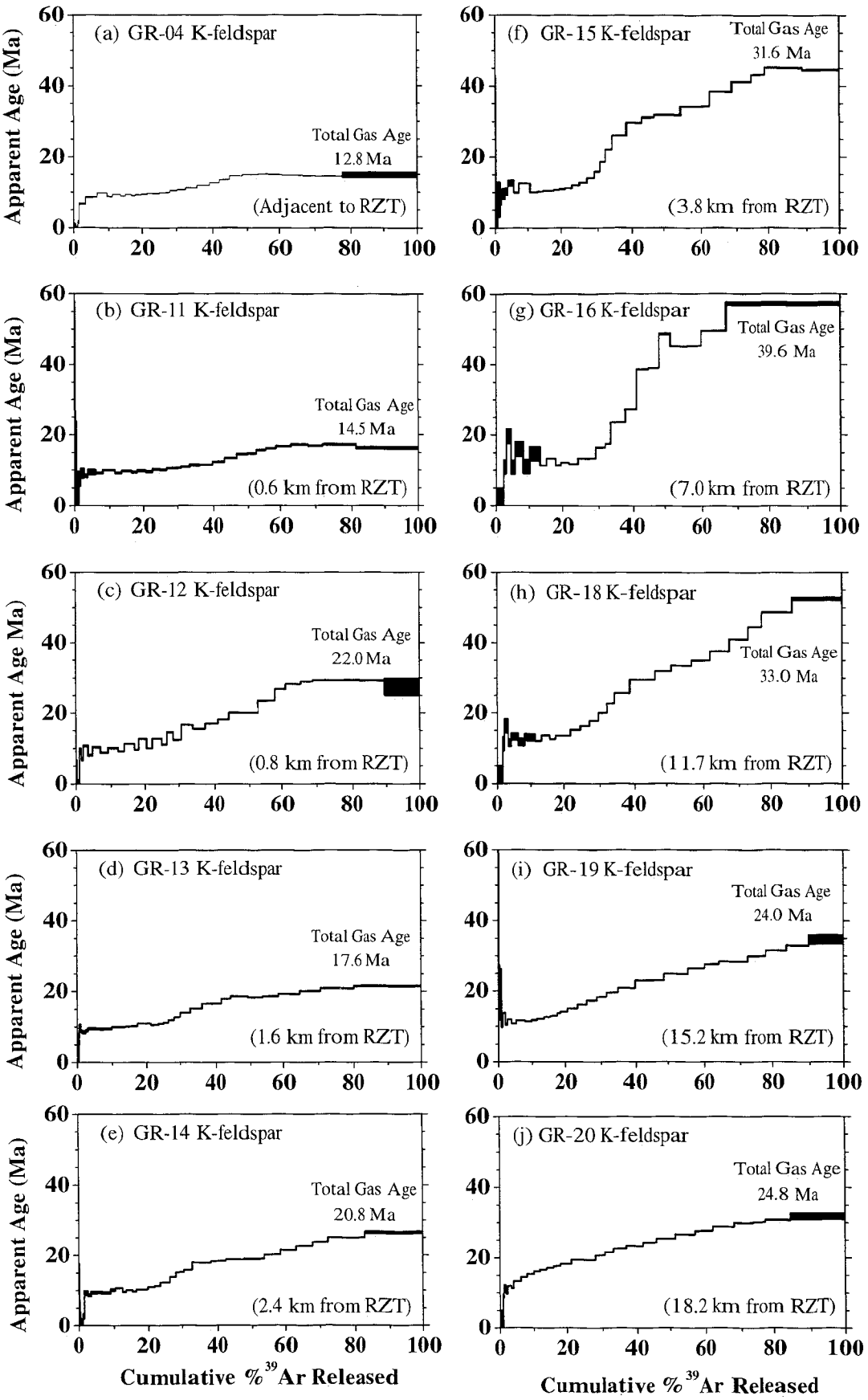

Figure 5. The $^{40}Ar/^{39}Ar$ age spectra of selected K-feldspars from the footwall of the RZT. Apparent ages corresponding to initial gas release have been corrected for Cl-correlated, excess ^{40}Ar (see text for details). Note strong equilibration of the initial gas released from all samples to apparent ages between 9 and 12 Ma. The total gas ages yielded by these samples are generally somewhat younger than those obtained from coexisting biotite.

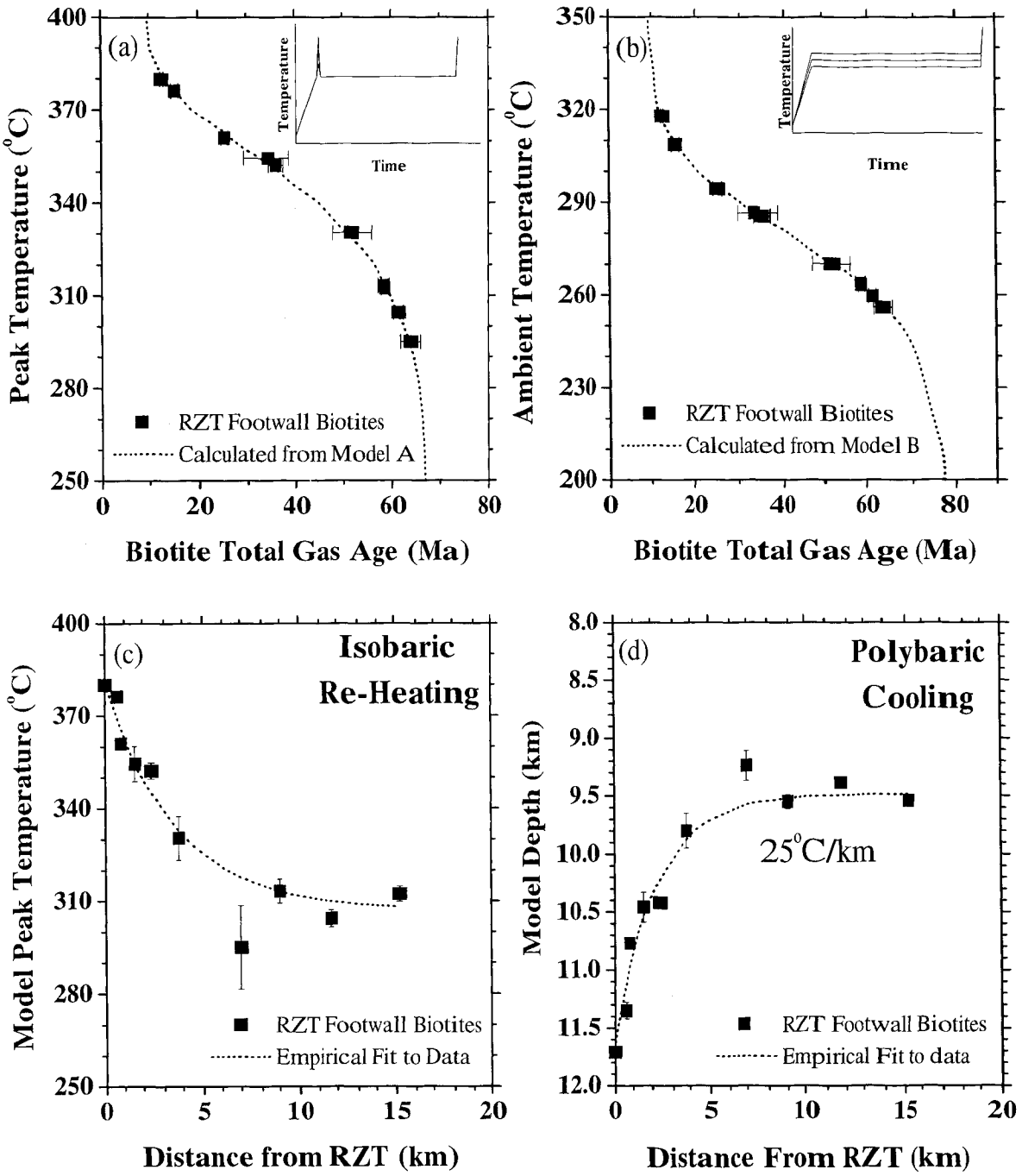

Figure 6. Possible interpretations of the relationship between biotite apparent age, sample depth, and distance from the RZT (assuming 25°C/km). (a) Relationship between biotite total fusion age and ambient temperature for samples residing at different depths (8-13 km) since the time of intrusion (~80 Ma) until 10 Ma (see inset). Calculations assume Ar diffusion parameters for biotite presented by Grove and Harrison [1996], cylindrical diffusion geometry, and an effective diffusion length scale of 150 μm. (b) Model depths of samples as a function of distance from the RZT constrained from their measured biotite total gas ages and interpolation from the relationship in Figure 5a above.

variable argon retention properties. In attributing this behavior to discrete distributions of noninteracting diffusion domains of varying dimension within K-feldspar, the MDD model broadly reconciles two distinct sources of information available from K-feldspar $^{40}Ar/^{39}Ar$ step-heating experiments: the age spectrum reflecting $^{40}Ar^{*}$ loss over geologic timescales, and the Arrhenius plot determined from the degassing systematics of reactor produced argon (principally, potassium-derived ^{39}Ar, or $^{39}Ar_K$) during laboratory heating. The $^{40}Ar/^{39}Ar$ age and ^{39}Ar diffusion results from a representative sample (GR-13 K-feldspar) are shown in Figure 7. The form of the Arrhenius plot $\log(D/r^2)$ versus $1/T$ (Figure 7b) is a function of the parameters that characterize the individual diffusion domains (activation energy (E), frequency factor (D_o), domain size (ρ), and volume fraction (ϕ)). Although the age spectrum (Figure 8a) also depends upon these parameters, its

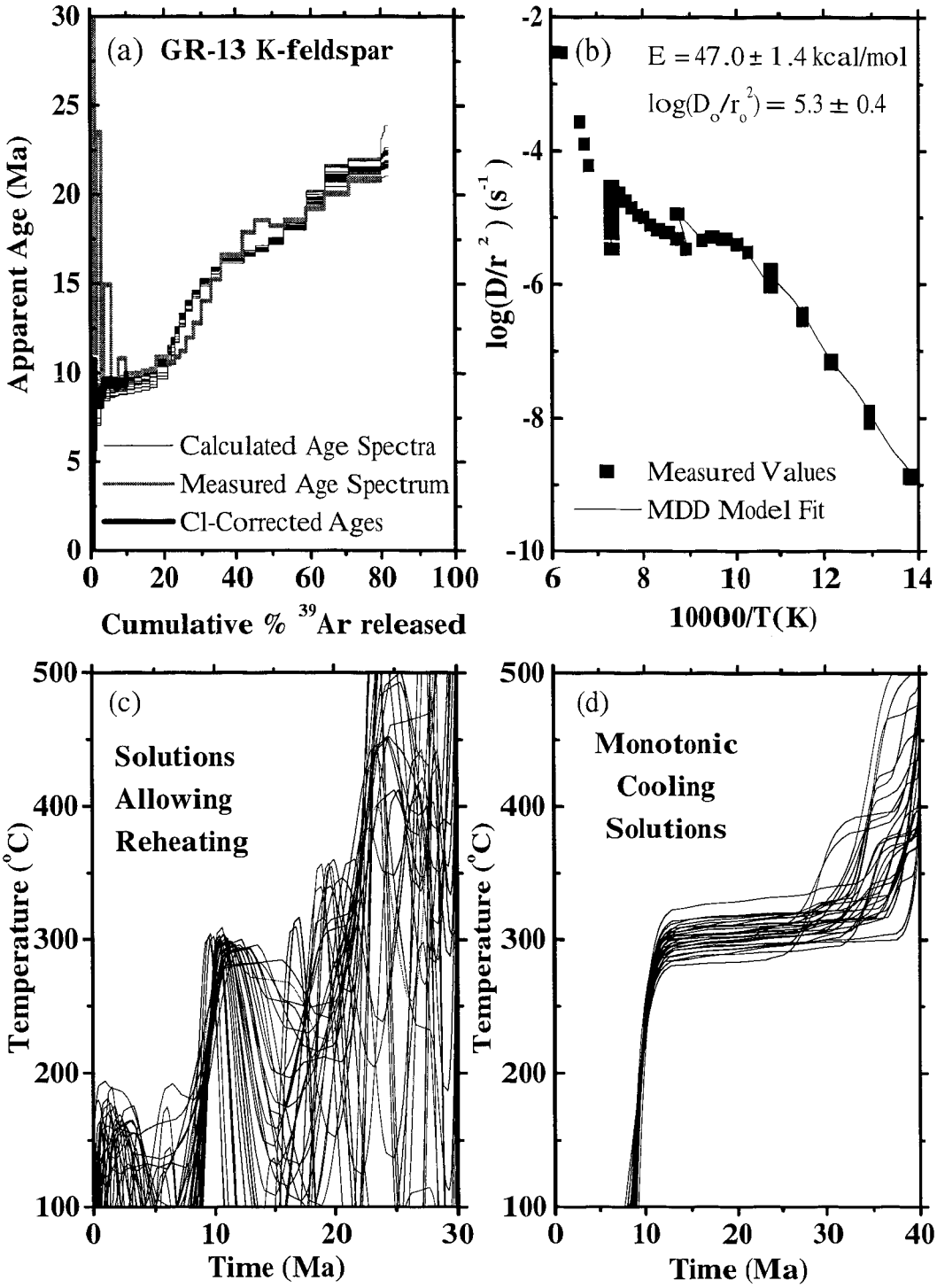

Figure 7. Thermal history results from GR13 K-feldspar are representative of most of the samples we have examined. (a) The measured age spectrum and model fits produced by bestfit thermal histories; (b) measured and model diffusion values calculated from ^{39}Ar diffusivities and the MDD model, respectively; (c) calculated thermal histories when reheating is permitted; and (d) calculated thermal histories assuming monotonic cooling. See text and Appendix C for details on how the curves were calculated and Plate 2 (solutions allowing reheating) and Plate 4d (monotonic cooling solutions only) for contours of the raw output data.

shape is farther modified by the thermal history. To the extent that diffusion parameters relevant to $^{40}Ar^*$ loss in nature can be determined at laboratory-required temperatures and timescales, the MDD model provides the basis for reconstruction of thermal histories over a broad temperature range (~150-350°C) applicable to the middle crust.

In this study, we have estimated both the domain distribution parameters and the thermal history through the use of nonlinear, least squares routines based upon the Levenberg-Marquardt method (Appendix C). Because our sampling strategy was predicated on the thermal effect of thrusting being the dominant control on the T-t histories in the footwall

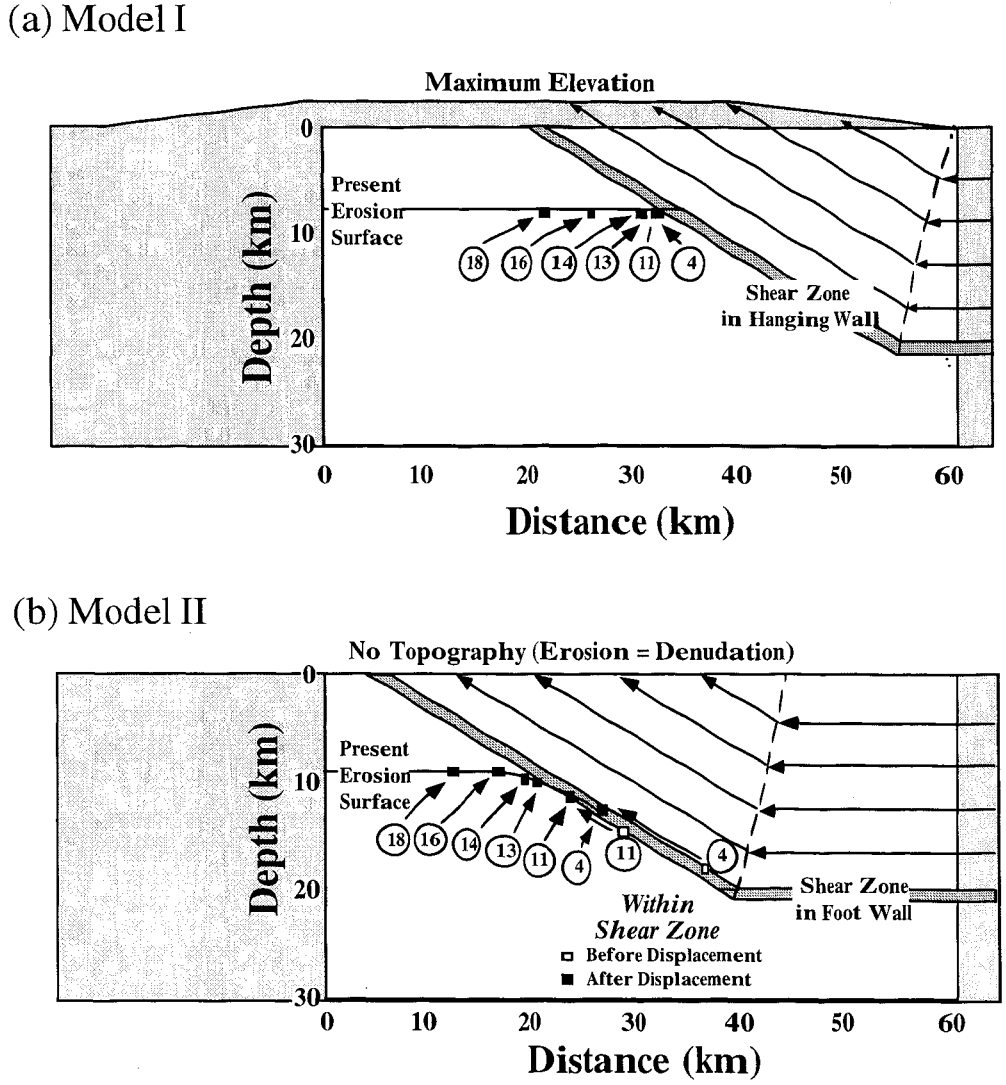

Figure 8. Schematic representation of grids used in the numerical heatflow calculations for the two different approaches attempted. The region for which calculations was performed is indicated in white. (a) Model I geometry showing isobaric array of samples and topographic effects simulated in the calculations by varying temperature at the surface. (b) Model II geometry illustrating the prefaulting and postfaulting positions of samples. Later denudation brings all samples to a common horizontal plane at 10 Ma.

we have permitted our K-feldspar thermal history solutions to record reheating. The increased freedom that results from permitting reheating to occur at any time produces a multitude of equivalent solutions, all of which are capable of reproducing the age spectrum of a given sample (e.g., 8c). Even so, the solutions tend to identify regions of T-t space where the thermal histories are tightly constrained by the sample. In contrast, solutions allowing only monotonic cooling tend to cluster tightly within the closure interval for Ar diffusion in K-feldspar (Figure 7d). Provided that a sample is known to have not experienced significant reheating, its entire thermal history can be closely constrained.

Solutions permitting reheating. We have constructed contour plots indicating the number of temperature-time solutions allowing reheating that pass through 30°C by 0.4 Ma elements of T-t space. As an example, the thermal history solutions obtained for GR-13 K-feldspar (Figure 7c) have been contoured in Plate 2. Contours of input thermal histories used in initiating the minimization process are shown in Plate 2a. To avoid biasing the results by the choice of input thermal histories, the densities shown in Plate 2a have been subtracted away from the bestfit results to obtain the contours shown in Plate 2b. Moreover, to facilitate intersample comparisons, the results have been normalized according to the number of solutions obtained so that plotted densities are equivalent for all samples. The highest-density shown (red) corresponds to a condition in which 45-50% of the curves pass through one of the grid elements. The lowest-density region (blue) corresponds to less than 3% of the solutions.

As indicated in Plate 2b, the results of calculations allowing reheating are generally tightly constrained only for regions of T-t space corresponding to the minimum age of the age spectrum. The additional argon retention that would occur for T-t histories encountering lower temperatures earlier on is compensated for by slightly higher (a few tens degrees Celsius) temperature at 10 Ma and vice versa. Because of this

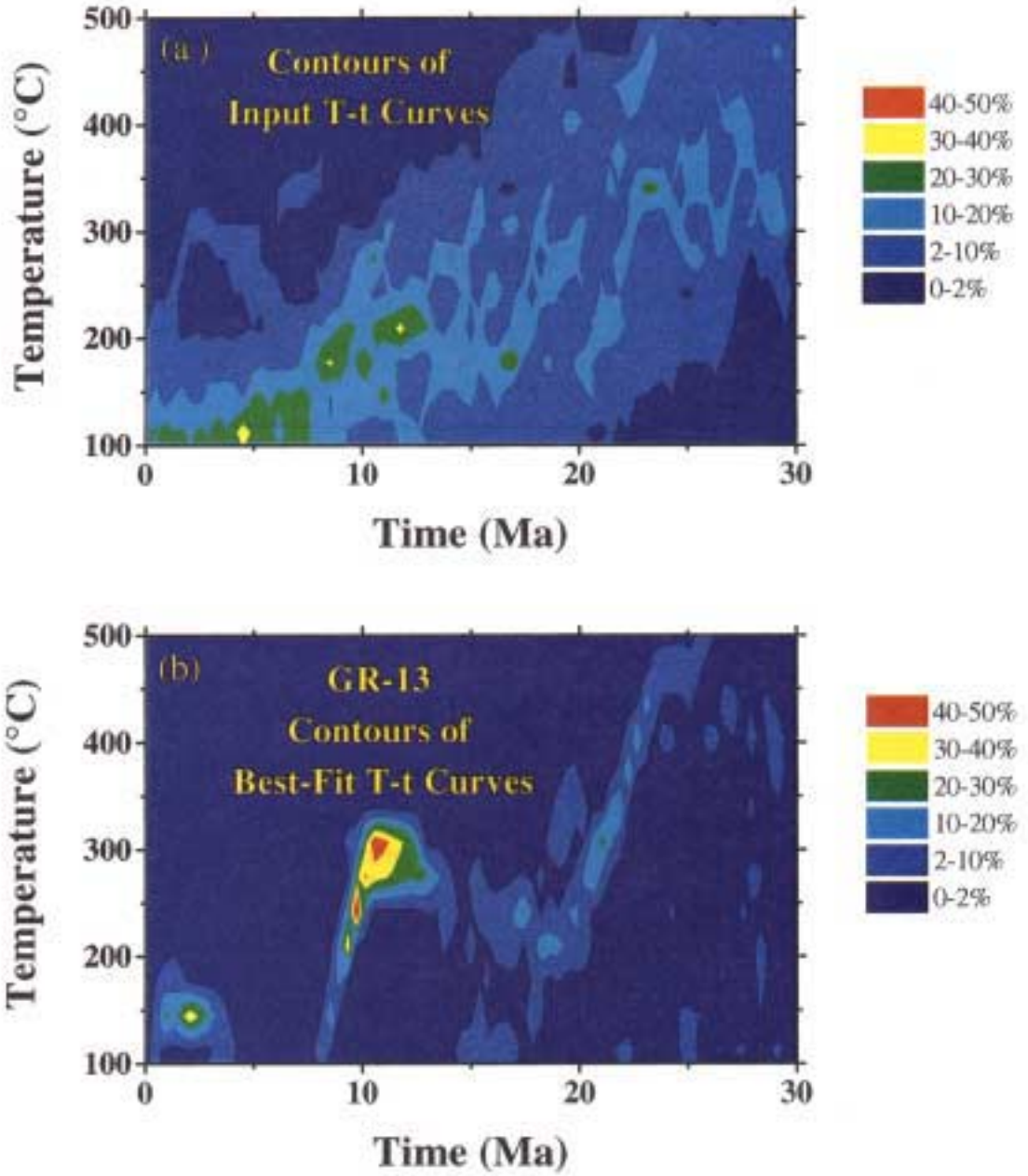

Plate 2. Contours of initial and bestfit thermal histories that allow reheating for GR-13 K-feldspar. The contours indicate the number of temperature-time histories which pass through 30°C by 0.4 Myr elements of T-t space. (a) Contours of the initial input thermal histories used to begin the fitting process. (b) The bestfit results. In both Plates 2a and 2b the highest densities (red) correspond to grid elements that contain greater than 45-51% of the T-t curves while the lowest (blue) have less than 3%. Note that to obtain the results shown in Plate 2b, density distributions for the initial input thermal histories shown in Plate 2a have been subtracted from the bestfit solutions.

property of our solutions, we have limited farther analysis of reheating results from the RZT footwall to the best defined region of temperature-time space (~15-5 Ma; Plate 3). All samples indicate that the maximum temperatures that could have been attained within this interval were ~320-280°C. Samples close to the RZT appear to indicate slightly higher temperatures (~320°C and a narrow peak centered at ~10 Ma (see GR-04 in Plate 3a). The resolution of the peak for more distal samples is degraded but appears to reach somewhat lower temperatures (see GR-18 in Plate 3f). Note that reheating to 280-320°C at ~10 Ma is only capable of explaining the initial portion of the age spectra yielded by our samples (<20% cumulative ^{39}Ar release). Observed differences in the age spectra at higher cumulative %^{39}Ar release (Figure 5) are not explained by reheating to 280-320°C at ~10 Ma. Although the latter point is treated in more detail in the discussion, we emphasize that if reheating at ~10 Ma is considered, a prior common thermal history at times older than 15 Ma cannot explain the age spectra yielded by all our samples.

Monotonic cooling solutions. To obtain monotonic

cooling solutions, we randomly selected activation energies (E) from a Gaussian distribution which described the magnitude and uncertainty of the experimentally determined value of E obtained from the step-heating results. Best fit domain distributions and thermal histories were then obtained as discussed in Appendix C. Results from our samples are indicated in Plate 4. For each of the samples we have calculated the 90% confidence interval for both the mean (indicated in black) and the overall distribution (indicated in yellow) of the cooling histories. Two salient features illustrated by Plate 4 include (1) an isothermal phase at ~270-290°C for samples removed horizontally by more than ~1 km from the trace of the RZT and (2) a rapid increase in the cooling rate for all samples at ~10 Ma.

Thermal History Simulations of Thrusting

In an effort to extract tectonic information from the K-feldspar thermal history results presented above, we have modeled the thermal evolution of the RZT using a two-dimensional, finite difference model which describes thrusting along a fault with a ramp-flat geometry (30° dip from 0 to 20 km; Figure 8) and a 600-m-thick shear zone. Two separate approaches have been adopted. The first (model I) allows heating of the footwall due to advection of the hanging wall, fluid flow, and frictional heating in the shear zone and heating due to an increase in topography created by slip on the ramp. Samples are maintained at constant depths in the footwall by confining the shear zone to the RZT hanging wall. The second (model II) involves only heat advection due to motion of the thrust hanging wall. Surface temperatures in model II were held constant with the erosion rate is set equal to the denudation rate (i.e., no net topography). In contrast to model I, portions of the footwall in model II are contained within the shear zone in order to allow us to explore the effect of different inital depths for the samples close to the RZT prior to faulting. The fundamental difference between the two models is that the first predicts significant reheating (>100°C) of the footwall, whereas the second does not (<10°C). Note that because the upper 600 m of the footwall are contained within the shear zone, samples adjacent to the fault actually experience a decrease in temperature as a result of shear strain which places them at shallower levels in the crust.

The calculation region for both models is 60 km wide by 30 km deep grid with a resolution of 600 x 600 points (Figure 8). The lateral limits and base of the grid were set far enough from the sample positions (shown in Figure 8) that they have negligible effect on the results. Other similarities between the two models include setting thermal diffusivity (10^{-6} m^2/s) and the initial geothermal gradient (25°C/km) at an average value for midcrustal rocks, maintaining constant temperature at the base of the grid (775°C at 30 km depth) and establishing a zero flux condition at the horizontal margins of the grid ($\partial T/\partial x = 0$ at $x = 0$ km and $x = 60$ km).

We approximated shear heating in the fault zone using viscous dissipation produced by simple Couette flow between parallel planar walls [*Turcotte and Schubert*, 1982, p. 234]. Because thrust faulting often produces abnormally high permeability and pore pressure in fault zones [e.g., *Hubbert and Rubey*, 1959], we have test the thermal effect produced by advecting fluid within the shear zone. In our model, fluid moves upward at a velocity that decreases exponentially with distance from the hanging wall. Darcy's law was used to estimate the effective permeability corresponding to each fluid velocity by assuming that the driving force was comparable to the lithostatic pressure gradient. Permeability is zero outside the limits of the shear zone.

Thermal effects resulting from the development of topography produced by upward motion of the hanging wall in model I were simulated by varying surface temperature. The latter was increased by an amount equal to the product of the change in elevation and the geothermal gradient. Note that because our data are only sensitive to the depth of the sample beneath the surface, we did not distinguish between the growth of topography at the surface due to thrusting and the resulting isostatic subsidence. Consequently, the topographic effects in Figure 9b refer to combined topography and subsidence. Development of topography in model I was linked to lateral displacement of the hanging wall. The erosion rate was set to increase linearly with elevation from zero at the datum elevation to a value equal to the denudation rate when a preset maximum elevation (see Figure 9b) was attained. Erosion continued at these rates after thrust displacements had ceased until all topography was eliminated.

The effects of varying the displacement rate, maximum elevation, and maximum permeability in model I for a sample position at the base of the shear zone (top of footwall) at a depth of 7 km are shown in Figure 9. As indicated in Figure 9a, relatively high displacement rates (above 10 mm/yr) are required to increase footwall temperatures by an amount (>30°C) that would be resolvable by K-feldspar thermochronology. The displacement rates required to produce this effect are reduced to the extent that locally developed topography of several kilometers insulates the footwall (Figure 9b). Fluid circulation within the shear zone is also highly effective in causing resolvable temperature increase in the footwall provided that maximum permeabilities are in excess of ~3 x 10^{-17} m^2 (Figure 9c). Frictional heating caused by very large shear stresses (100-200 MPa) produces a similar effect (Figure 9d). Because fluid circulation, frictional heating, and topography are not considered in model II, calculated thermal histories are only weakly influenced by lateral heat conduction from the hanging wall and thus depend primarily upon starting depths.

Discussion

Thermal Effect of Displacement Along the RZT

The clearest inference we can draw from our results is that the systematic variation in the K-feldspar age spectra (Figure 5), and to a lesser extent the biotite ages (Figure 4), as a function of distance from the trace of the RZT strongly implicates the fault in creating the observed age distributions. The enhanced thermal history information that can be recovered from K-feldspar step-heating experiments permits us the potential to distinguish between two distinct kinds of thermal histories, monotonic cooling and those involving reheating. Although biotite ages can be predicted for both types of histories (see Figure 6), the inability of the $^{40}Ar/^{39}Ar$ method to reveal internal Ar distributions and kinetic properties of micas does not allow the form of the geological thermal history to be directly assessed.

Accordingly, we have developed two contrasting models for the tectonic evolution of the RZT that are both capable of predicting significant aspects of the thermal history results (Figure 8a). Model I emphasizes the partial isotopic reequilibration of all samples at relatively shallow depths

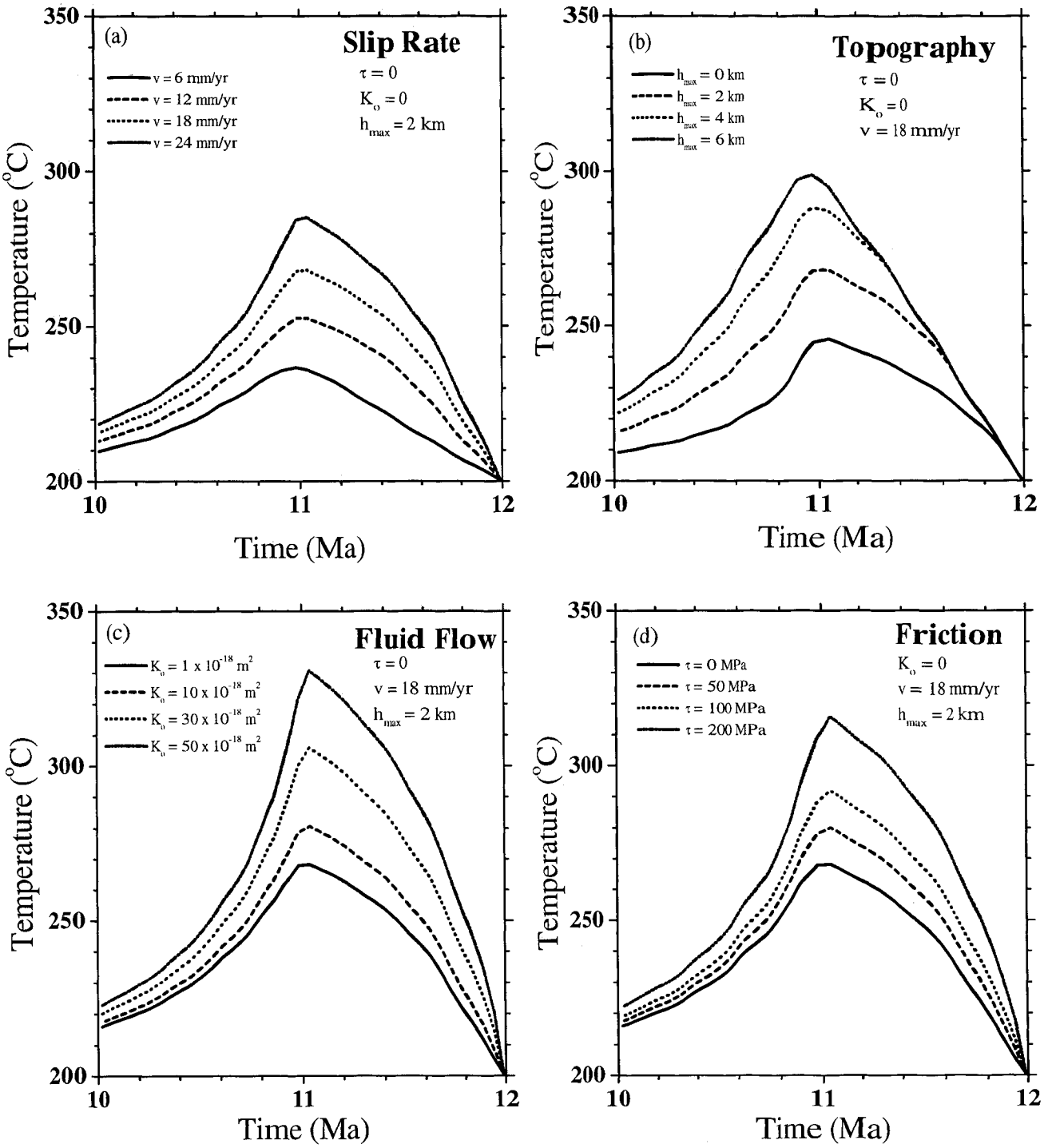

Figure 9. Representative results from the numerical heat flow calculations for a sample position in the footwall immediately adjacent to the fault. The thermal effects of varying (a) the slip rate, (b) net topography and isostatic subsidence, (c) advective heat transport due to fluid flow, and (d) amount of frictional heating. Note that calculations are performed for constant values of other parameters shown on the figures. See text for additional details.

(corresponding to temperature of ~150°C) due to a thermal event at ~12-10 Ma resulting from tens of kilometers displacement along the RZT at that time (Figure 10a). This event creates a strong temperature pulse that resets the smallest domains of most K-feldspars, including those at ~6 km from the RZT (Figure 10; see also Plate 3). The magnitude of the thermal excursion necessary to raise the temperature of the zone more than 100°C requires not only significant displacement along the RZT (~15-20 mm/yr for ~2 Myr) but also combined topography and subsidence of ~5 km that must be rapidly irradicated by combined denudation and erosion (Figure 8a) in order for samples to return temperatures to their

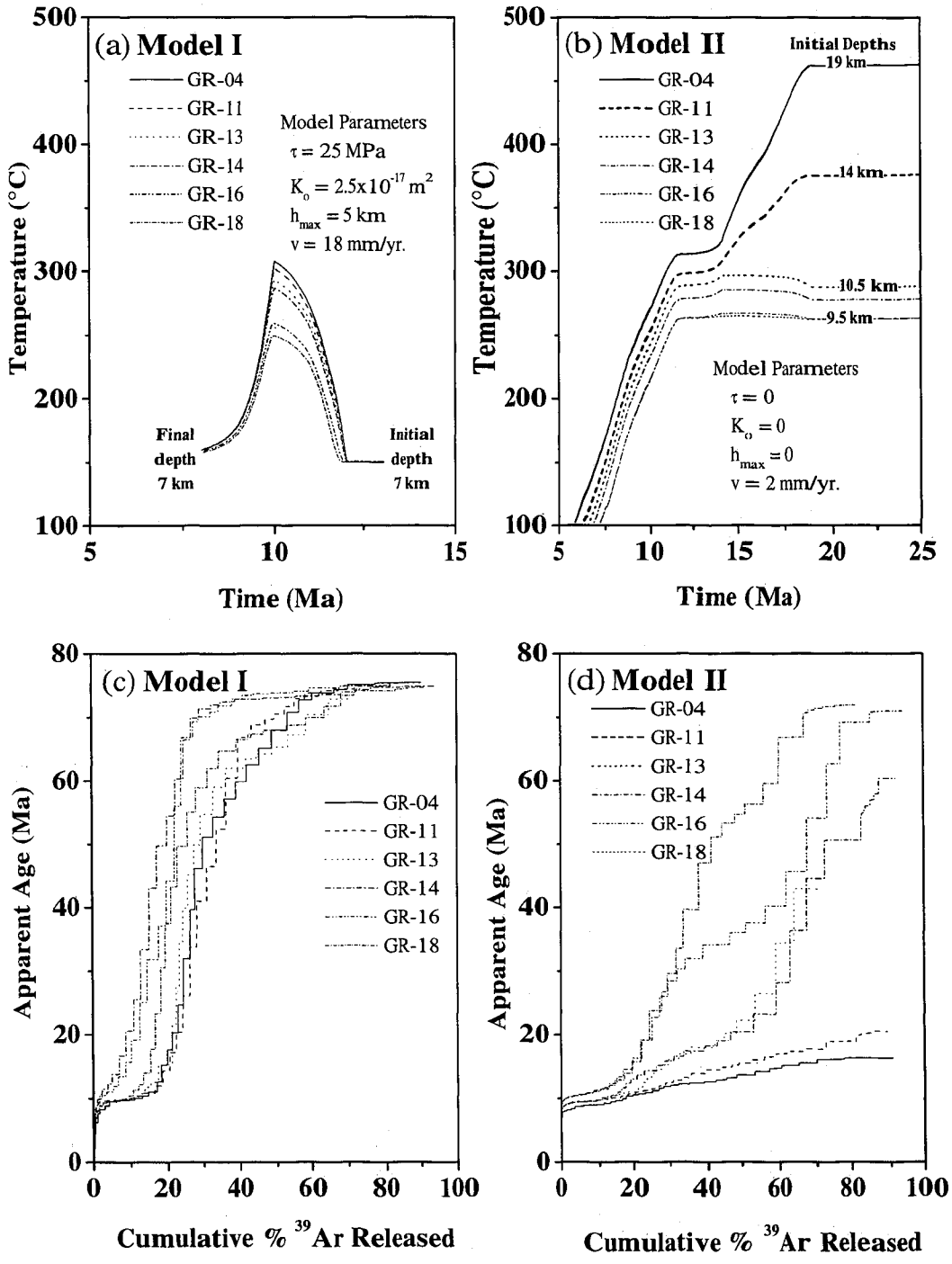

Figure 10. Results of the heat flow calculations. (a) Model I results for isobaric sample positions at progressively greater distances from the RZT (see Table 1). Values of 18 mm/yr, 25 MPa, 2.5 x 10^{-17} m^2, and 5 km were used for displacement rate, shear stress, shear zone permeability, and combined topographic increase and isostatic subsidence, respectively. Model results for individual samples have been superposed on Plate 3. (b) model II results sample positions that vary in depth with time as a result of fault drag and post faulting denudation (see Figure 8). The RZT moves at 2 mm/yr between ~19 and 14 Ma (~12 km total displacement). GR-04 and GR-11 move upward to 11.5 km from 19 km and 14 km depths, respectively, due to drag along the RZT. Samples GR-04 to GR-14 exhumed differentially during later denudation at 10 Ma. (c) and (d) Model age spectra calculated produced for our samples from model I and model II, respectively. Model results for individual samples have been superposed on Plate 4.

ambient values (i.e., ~150°C at ~9 Ma). Fluid circulation and friction cannot be the dominant heat sources in raising the temperature of the zone as they produce a very local effect which rapidly decays with distance, in contrast with the more regional effect we observe in our samples (Plate 3).

Although a heating pulse to ~320-280°C at ~10 Ma does explain the Ar loss in the first 10-15% of ^{39}Ar released in all age K-feldspar spectra (Figure 10c), it does not provide insight into the prior thermal history. In fact, it is difficult to reconcile the relatively young and systematically increasing ages of the largest domains of the K-feldspars (Figure 5) with shallow intrusion of the granitoids (<5 km) at ~80 Ma followed a single event at ~10 Ma. Another shortcoming of the reheating model is that it is not compatible with the distribution of biotite ages. The temperature increase required to reproduce this age distribution (Figure 6c) is >50°C higher than that which would only reset the smallest domains of the K-feldspar (Plates 3a-3f). In contrast with the observations (Figure 5), reheating to 380-400°C would reset more than 60% of the gas in the K-feldspars to ages of ~10 Ma.

The K-feldspar thermal history results are more completely explained by a model in which the footwall samples close to the trace of the RZT originated at much greater depths (~12-9 km) and denudation of the region occurred at ~10 Ma (Figure 8b). The timing of initial upward displacement of the RZT hanging wall is constrained to be ≥18 Ma from the hornblende ages (Figure 3) and the two K-feldspar samples closest to the fault. GR-04 and GR-11 are inferred to have been brought up from the greatest depths (and this highest temperatures) explaining why their entire age spectra yield ages <18 Ma. A relatively small displacement (~12 km) on the RZT between ~19 and 14 Ma is capable of explaining the age spectra of samples close to the fault but have little effect on modifying K-feldspar age spectra at distance greater than ~3 km from the fault (Figure 10; see also Plate 4). Note that these two samples are distinct from the others in having been ductilely sheared under greenschist facies. The age spectra of samples at >3 km distance from the RZT are better explained by constant ambient temperatures (~260-290°C) following emplacement at ~80 Ma. This interpretation is also consistent with the pattern of biotite ages (see Figure 6). The differential emplacement position of the samples required to explained their age spectra implies that a small rotation of the shear zone (~5°) occurred during denudation of the fault zone which brought the samples to the surface today (Figure 10d). Such a rotation can be explained by enhanced isostatic rebound in the south as a result of higher topography that formed there during faulting.

Timing and Sequence of Thrusting Within the Himalaya and Southern Tibet

The models we consider are both consistent with slip along the RZT near Lang Xian occurring between 19 and 11 Ma. This is in accord with the earlier suggestion that the RZT was active near Renbu at 17.5±0.9 Ma [*Ratschbacher et al.*, 1994]. Our preferred interpretation is that the overriding Tethyan plate produced relatively little thermal effect on the footwall granitoids but variably transposed samples adjacent to the thrust. While the slip rate calculated from this model of ~2 mm/yr is low compared to the modern convergence rate of the MHT of 16±4 mm/yr [*Bilham et al.*, 1996], this is constrained primarily by drag within the footwall and is thus likely to be highly underestimated. Alternatively, the slip rate required to explain the footwall thermal histories in terms of a thermal pulse is of the order of ~10-20 mm/yr. Available geological and geophysical evidence suggests that the RZT may sole into a subhorizontal midcrustal decollement at depth [*Makovsky et al.*, 1996; *Yin et al.*, 1994]. Within the framework of the reheating model (model I), the thermochronologic results record the effect of the thermal contrast produced by juxtaposing contrasting structural levels. It follows that any slip occurring along a subhorizontal midcrustal surface reduces the potential thermal contrast, leaving a diminished record that would be difficult to detect by our method. Thus the actual slip rate and magnitude of displacement could be greater than we have calculated for the RZT. The timing of initiation of faulting, however, is not affected by this limitation.

The pattern of thrust activity in the Himalaya and southern Tibet is not well understood, but some details are emerging. The Gangdese Thrust, the earliest identified crust thickening event, is believed to have been active between 27 and 23 Ma [*Yin et al.*, 1994; T.M. Harrison, unpublished data, 1996]. The Main Central Thrust is thought to be responsible for production of the High Himalayan leucogranites which range in age from 24 to 19 Ma [*Harrison et al.*, 1995b; *Coleman and Parrish*, 1995] and suggest a late Oligocene to early Miocene age for the initiation of MCT activity [also see *Hubbard and Harrison*, 1989]. Recently, *Harrison et al.* [1996] recognized a reactivation of the MCT beginning during the late Miocene and continuing into the Pliocene. Activity on the Main Boundary Thrust is inferred from magnetostratigraphic investigations of the Himalayan foreland to have initiated at ~11 Ma [*Burbank et al.*, 1996]. Our inference that the Renbu Zedong Thrust was active in the interval 19-11 Ma places this feature out of sequence in an otherwise general pattern of propagation of south directed thrusts toward the foreland. However, it does fills a gap in time that is not represented by current estimates of the timing of the other recognized thrust faults.

A possible kinematic link with Himalayan structures is raised by the recent observation that the South Tibetan Detachment System (STDS) [*Burchfiel et al.*, 1992] was active in the eastern Himalaya at 12.5±0.3 Ma [*Edwards et al.*, 1995]. It is possible that in this part of the collision zone, the STDS and RZT are mechanically linked. Specifically, extension in the High Himalaya was accommodated by contraction in southern Tibet along the RZT [*Yin et al.*, 1994].

Although the rapid cooling event at ~10 Ma is documented in every K-feldspar thermal history (Figure 7), late Miocene cooling ages were not documented in a detailed thermochronological study ~250 km farther west within the Gangdese batholith [e.g., *Copeland et al.*, 1995]. The sampled transect in the present study is unusual in both its proximity to the eastern syntaxis (Figure 1) and the fact that at 29°N latitude, it represents by far the most southerly exposure of the Gangdese batholith. It seems unlikely that these young cooling ages reflect tightening of the Himalayan arc near the syntaxis as K-Ar ages immediately adjacent to the Namche Barwa metamorphic complex yield early Miocene ages [*Nievergelt et al.*, 1995]. The southerly extent of the batholith and the higher grade of metamorphism of the upper plate rocks indicate a deeper level of exposure than is typical farther west along strike. Although this endows the isotope systems of these

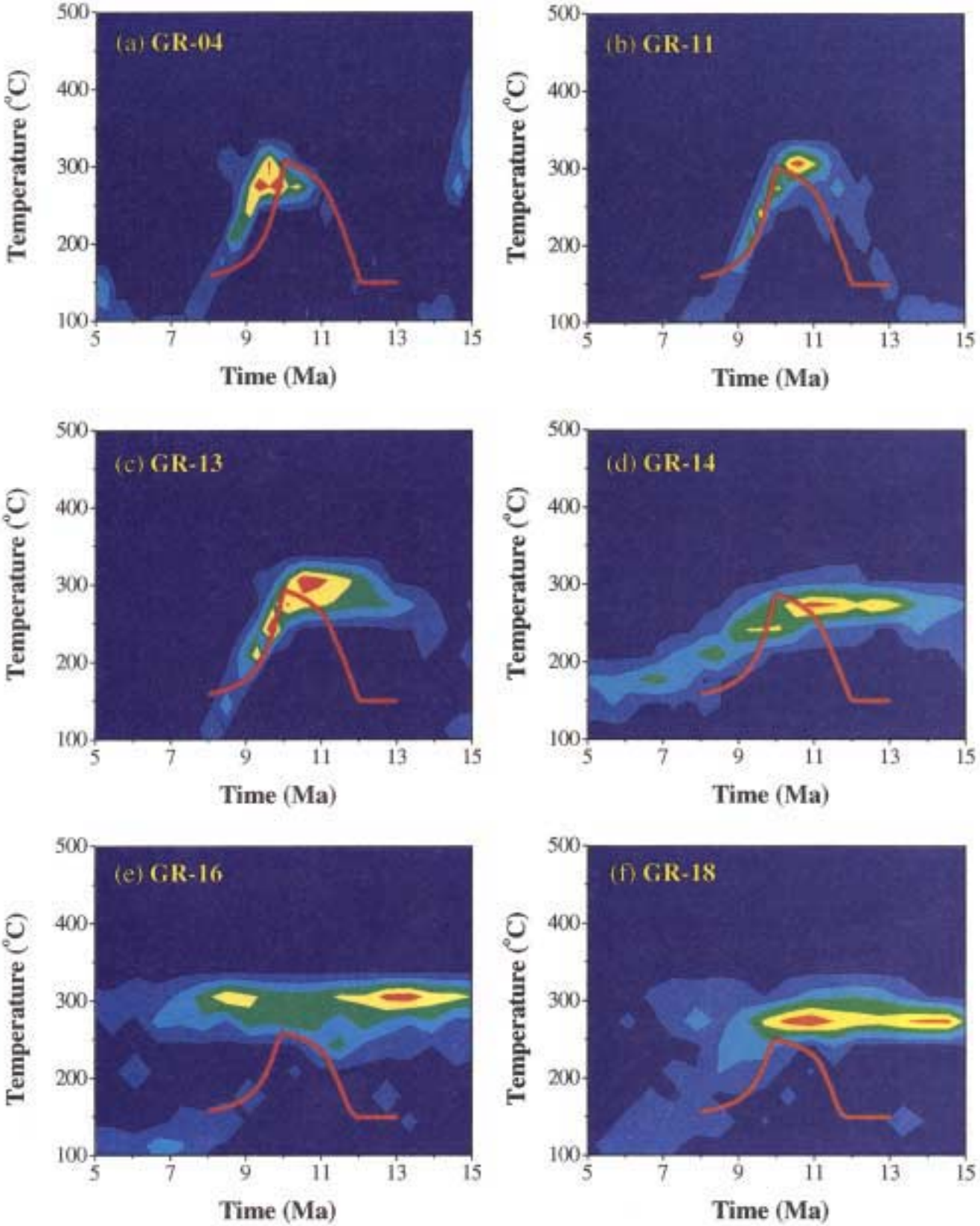

Plate 3. Contours of bestfit thermal histories allowing re-heating for selected samples: (a) GR-04; (b) GR-11; (c) GR-13, (d) GR-14; (e) GR-16; and (f) GR-18. Note that the densities of bestfit temperature-time histories have been normalized to account for different numbers of solutions obtained for each sample. Results are shown only for the time interval 5-15 Ma. At earlier times, the possible T-t distributions capable of explaining the age spectra of most samples is poorly constrained. The red curves were produced from numerical heat flow calculations described later in the text (see Figure 10).

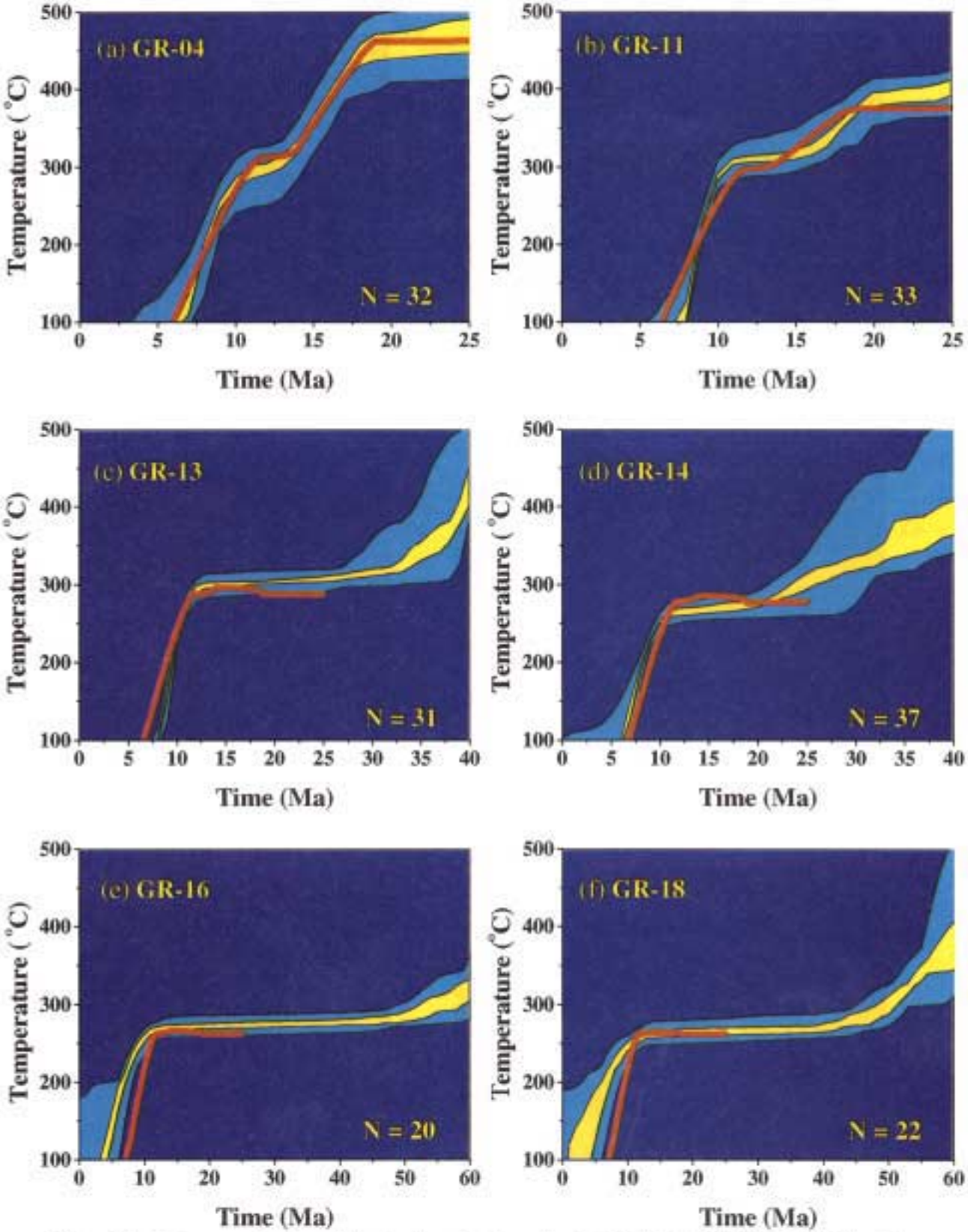

Plate 4. Bestfit monotonic thermal histories for selected samples: (a) GR-04. (b) GR-11. (c) GR-13. (d) GR-14. (e) GR-16, and (f) GR-18. The 90% confidence intervals for the mean (medium-gray shaded region) and overall distribution (light-gray shaded region) have been calculated for each sample on the basis of 20 or more thermal histories. Variation in the thermal histories primarily reflects uncertainty in E (see text for details). Model age spectra calculated from these thermal histories using the MDD model approach generally match the measured age spectrum of the sample to within ±1 Myr for cumulative ^{39}Ar release between 0% and that corresponding to melting (typically 75% gas release). The number of solutions obtained for each of the samples is indicated in the upper right hand of each plot. The red curves were produced from numerical heat flow calculations described later in the text (see Figure 10).

rocks with a greater potential for remaining open to record thermal disturbances at later times than the shallower rocks farther west, it does not explain the cause of the sudden onset of cooling. Several observations, however, may bear upon this question.

Results of seismic reflection profiling in southern Tibet [*Makovsky et al.*, 1996] have been interpreted as indicating that all the Himalayan thrusts sole into a common decollement, the Main Himalayan Thrust [*Zhao and Nelson*, 1993] which extends well into southern Tibet. *Hauck et al.* [1995] speculate that the MCT must steepen its northward dip somewhere beneath the suture zone as it is not resolved farther north under the Gangdese batholith. The RZT has been imaged in these seismic experiments and its geometry at depth is consistent with it linking to either the MHT or South Tibetan Detachment System (STDS). If the RZT was a backthrust of the MHT, then it is conceivable that activity on the MHT between ~19 and 11 Ma bypassed the MHT ramp and was instead accommodated by the RZT. If the MHT does dip steeply to the north under southern Tibet [*Hauck et al.*, 1995], then the suture zone region would have been rapidly uplifted, denudated, and cooled following initiation of the MBT and/or reactivation of the MCT at ~11 Ma.

Conclusions

Near Lang Xian, southeastern Tibet, the Renbu Zedong Thrust places epidote-amphibolite facies Tethyan metasediments atop the Gangdese batholith. U-Pb zircon results indicate that this portion of the batholith was emplaced between 100 and 70 Ma with most intrusions formed at ~85 Ma. K-feldspar and biotite $^{40}Ar/^{39}Ar$ results from a NW-SE transect through footwall granitoids reveal disturbances to their isotopic systems immediately beneath the RZT. This effect systematically decreases with increasing distance from the RZT. Inverse modeling of the K-feldspar $^{40}Ar/^{39}Ar$ results yields thermal history data that indicate that the RZT was active in the interval 19-11 Ma. In conjunction with a numerical thermal model, the results constrain the minimum average slip rate and displacement along the ramp between 19 and 15 Ma to be 2 mm/yr and 12 km, respectively, but were likely higher. A cooling episode recorded by all the K-feldspar age spectra beginning at ~10 Ma may either reflect denudation following regional uplift due to displacement along a ramp on the Main Himalayan Thrust or topographic collapse following cessation of RZT thrusting. RZT activity between 19 and 11 Ma places this backthrust out of the generally southward progression of thrusting but occupies a period that appears to otherwise be unrepresented by contractional motion in the Himalaya.

Appendix A: U-Pb Zircon Ion Microprobe Techniques

The UCLA CAMECA ims 1270 ion microprobe was utilized in the determination of U-Pb zircon ages. A survey of experimental conditions [*Schuhmacher et al.*, 1994] identified an operating mode which optimized Pb sensitivity while yielding reproducible interelement ratios. All results reported here are on separated zircon grains mounted in epoxy, polished to 0.3 μm alumina, and coated with ~100 Å of Au using a sputter-coater. The standard operating conditions used for analyses presented in this paper are O_2^- primary beam focused to a ~15 x 20 μm spot, a mass resolving power (MRP) of about 5500, a 50 eV energy window, and a 15 eV offset for $^{238}U^+$.

Molecular ions in the 204 to 208 mass range have the potential to interfere with the Pb peaks and require the use of high MRP. High-resolution mass spectra of zircons show that the principal interference is $^{176}Hf^{28}Si^+$ at mass 204 which can be separated from the ^{204}Pb using an MRP of about 5500. Instrumental mass discrimination of Pb isotopes is not detectable at the per mil level [also see *Compston et al.*, 1984]. Tests using Mud Tank zircon ($^{206}Pb^*$ = 0.9±0.1 ppm (R.R. Parrish, personal communication, 1992)) indicate ion yields of up to 25 cps/ppm Pb^+/nA O_2^- for primary ion beams of <5 nA. Enhanced ionization efficiencies of up to 100% for Pb^+ from zircon under O_2^- bombardment can be accomplished by O_2 flooding [*Schuhmacher et al.*, 1994].

Because of the contrasting energy distributions of $^{206}Pb^+$ and $^{254}UO^+$ with respect to $^{238}U^+$ [*Schuhmacher et al.*, 1994], a plot of $^{254}UO^+/^{238}U^+$ *versus* $^{206}Pb^+/^{238}U^+$ for a homogenous standard yields a linear array allowing a correction factor to be derived by dividing the measured $^{206}Pb^+/^{238}U^+$ of a standard zircon at a reference $^{254}UO^+/^{206}U^+$ value by its known daughter to parent ratio. The age of an unknown, measured under identical conditions, can then be determined by applying this relative sensitivity factor. We used zircon AS-3, which yields concordant $^{206}Pb/^{238}U$ and $^{207}Pb/^{235}U$ ages of 1099.1±0.5 Ma by isotope dilution/thermal ionization mass spectrometry [*Paces and Miller*, 1993], as the standard for these analyses.

Because of the relative youth and low U contents of our zircons, we routinely utilized oxygen flooding in analysis of the Gangdese granitoid zircons to increase Pb^+ yields. We found that a ~20-min measurement cycle yielded $^{206}Pb/^{238}U$ ages with ±2% precision. This uncertainty primarily reflects the variability in the $^{254}UO^+/^{238}U^+$ *vs.* $^{206}Pb^+/^{238}U^+$ calibration for these comparatively young (Cretaceous) samples provided that they are sufficiently (>80%) radiogenic.

Appendix B: $^{40}Ar/^{39}Ar$ Methods

High purity concentrates of K-feldspar, hornblende, and biotite were irradiated for 45 hours in the L67 position of the Ford Reactor, University of Michigan. Variation in the J factor determined from Fish Canyon sanidine (27.8 Ma) flux monitors for all samples was between 0.0067 and 0.0068. Correction factors for interfering neutron reactions determined from K_2SO_4 and CaF_2 included with the samples were $(^{40}Ar/^{39}Ar)_K$= 0.0246, $(^{38}Ar/^{39}Ar)_K$ = 1.21 x 10^{-2}, $(^{39}Ar/^{37}Ar)_{Ca}$ = 7.89 x 10^{-4}, and $(^{36}Ar/^{37}Ar)_{Ca}$ = 2.63 x 10^{-4}. Biotite flakes were fused with a continuous 5-W Ar ion laser to obtain total fusion ages. K-feldspar (~30 mg aliquots of ~0.7 mm grains) and amphibole samples (~20-mg aliquots) were step heated in a Ta crucible within a double vacuum furnace. The $^{40}Ar/^{39}Ar$ isotopic measurements were performed using either a VG 3600 or VG 1200S automated mass spectrometer. Representative cold extraction line blanks for m/e 40,39, and 36 were 1-2 x 10^{-16}, 0.7-1.0 x 10^{-18}, and 3-5 x 10^{-18} mol ^{40}Ar, respectively, for both extraction lines. Hot furnace blanks were <1 x 10^{-15} mol ^{40}Ar below 1100°C. Large gas fractions admitted to the VG 3600 were typically measured using a Faraday detector (^{40}Ar sensitivity of 2 x 10^{-15} mol/mV) to measure mass 40 and 39 and a Daly photomultiplier (gain of ~100 over the Faraday detector) to determine m/e 39 through 36. Detector gain was calibrated in each analysis with common measurements on m/e 39 and measured mass discrimination values for

both detectors. Experiments performed with flux monitors ($^{40}Ar/^{39}Ar \sim 1$) indicate that corrected $^{40}Ar/^{39}Ar$ ratios determined using the two detectors are identical within analytical uncertainty to those calculated from measurements using only the photomultiplier. Additional experimental are given by *Harrison et al.* [1991] and *McDougall and Harrison* [1988]. Tabulated results of the argon isotopic analyses calculated using conventional decay constants and isotope abundances, uncorrected for neutron produced interferences, are available on the WWW at http://oro.ess.ucla.edu/argon.html.

Appendix C: Use of Levenberg-Marquardt Methods in the MDD Model

The Levenberg-Marquardt method is a widely used approach in least squares analysis of nonlinear problems [*Press et al.*, 1988]. As in conventional leastsquares analysis, a merit function (χ^2) is defined. Minimization of χ^2 using Levenberg-Marquardt is accomplished by smoothly varying between the extremes of the inverse-Hessian method and the method of steepest descent [*Press et al.*, 1988]. In applying this calculation scheme, we have supplemented Press et al.'s subroutines with algorithms to calculate the functions for fitting the ^{39}Ar and $^{40}Ar^*/^{39}Ar_K$ data and their derivatives. The expressions employed appear in Appendixes B and C of *Lovera et al.* [1989] and include the cumulative fraction of ^{39}Ar released, (^{39}f, equation C1 of *Lovera et al.* [1989]) and the age corresponding to the mth heating step (age_m, equations B2-B5 of *Lovera et al.* [1989]).

After obtaining values for E and $\log(D_0/r_0^2)$ by applying a least squares fitting to the initial low-temperature Arrhenius data [*O. M. Lovera et al.*, manuscript in preparation, 1996], the volume fraction (ϕ_i) and the relative size (ρ_i) of each domain are varied to fit the expression for ^{39}f. The variational method employed in the Levenberg-Marquardt is starting by supplying an initial set of parameters that will be varied iteratively to minimize the χ^2. Derivatives of ^{39}f with respect to individual parameters are calculated in a straightforward manner from the expression given by *Lovera et al.* [1989]. The routine is halted after three sucessive iterations in which the fractional decrease in χ^2 is <0.001. Since the function is nonlinear, different initial sets of parameters may converge upon different solutions which satisfy the minimization criteria. For the fitting of the ^{39}Ar laboratory data, it has previously been established that nonuniqueness of the estimated domain distribution will not affect the resulting determination of the thermal history provided that the domain distribution parameters provide an adequate description for Ar diffusion in the sample [*Lovera et al.*, 1990].

This variational process described above may be repeated for different numbers of domains in order to obtain the best solution. Normalization (i.e., $\sum \phi_i = 1$ and $\rho_{max} = 1$) reduces the number of free variables by two. In addition, only positive values of ϕ_i and ρ_i are permitted by the MDD model. Note that in order to avoid singularities of the Hessian matrix, no more than 20 orders of magnitude are allowed to exist between the sizes or volume fractions of domains.

Once the diffusion properties (E, D_0) and the domain distribution (ρ_i, ϕ_i) are determined, the only unknown in the age function [equations B2-B3 of *Lovera et al.*, 1989] is the thermal history. To model the $^{40}Ar/^{39}Ar$ data using the Levenberg-Marquardt method, an expression for the thermal history must be given in order to calculate age_m. In our approach, variation of age_m is accomplished by changing the parameters that define the thermal history which we express as a Chebyshev polynomial, $P_k(t)$:

$$T(t) = \sum_{k=1}^{N} a_k P_{k-1}(t) - \frac{a_1}{2}, \quad P_k(t) = \cos(k \arccos(t))$$

We have found that an expansion of order N≈10-20 is sufficient to adequately represent any thermal history. Lower-order expansions lack sufficient resolution while those of larger order consume unnecessary computing time. We employ two primary approaches in constraining possible thermal histories. These include (1) monotonic cooling only ($\partial T/\partial t \leq 0$ for all t); and (2) more general histories that permit reheating (no constraint on $\partial T/\partial t$). Because T(t) in the age_m expression is highly nonlinear, expressions for the partial derivatives of age_m were calculated numerically using a finite difference approach. In both instances, we satisfied the MDD model requirement of intial zero ^{40}Ar by beginning cooling histories at sufficiently high temperatures (600°C) to guarantee no quantitative ^{40}Ar accumulation. Applying this constraint leaves n-1 free coefficients in the Chebyshev expansion. Similar restrictions for the variation of parameters and stopping criteria described for ^{39}f above were imposed. We have found that the monotonic cooling constraint is sufficient to define an effectively unique cooling history within the laboratory uncertainty. This is not the case for the general thermal histories case however, where multiple valid solutions are usually obtained. Additional documentation, compiled programs and FORTRAN source code for the routines described above are available from the WWW site mentioned in Appendix B.

Acknowledgments. This work was supported by grants from the DOE, NSF, and the Lawrence Livermore National Laboratory Collaborative University Projects. Our work in southern Tibet was aided by Xinhua Zhou (Academica Sinica) and Chen Wenji (State Seismological Bureau). We thank Bayi Gong An for providing directional assistance.

References

Allègre, C.J., et al., Structure and evolution of the Himalaya-Tibet orogenic belt, *Nature, 307*, 17-22, 1984.

Baldwin, S.L., T.M. Harrison and J.D. Fitz Gerald, Diffusion of $^{40}Ar/^{39}Ar$ in metamorphic hornblende, *Contrib. Mineral. Petrol., 105*, 691-703, 1990.

Bilham, R., K. Larson, and J. Freymuller, India/Tibet convergence rate from 1991-1995 geodetic measurments in the Nepal Himalaya, paper presented at the 11th Himalayan-Karakorum-Tibet Workshop, Flagstaff, Ariz. April 29 to May 1, 1996.

Bouchez, J.L., and A. Pêcher, Himalayan Main Central Thrust pile and its quartz-rich tectonites in central Nepal, *Tectonophysics, 78*, 23-50, 1981.

Burbank, D.W., R.A. Beck, and T. Mulder, The Himalayan foreland basin, in *The Tectonics of Asia,* edited by A. Yin and T.M. Harrison, pp. 149-188, Cambridge Univ. Press, New York, 1996.

Burchfiel, B.C., Z. Chen, K.V., Hodges, Y., Liu, L.H., Royden, C. Deng, and J. Xu, The South Tibetan Detachment System, Himalayan orogen: Extension contemporaneous with and parallel to shortening in a collisional mountain belt, *Spec. Pap. Geol. Soc. Am., 269*, 1-41, 1992.

Burg, J.P. (Compiler), Carte géologique du sud du Tibet, scale 1:500,000, Cent. Natl. de la Rec. Sci., 1983.

Burg, J.P., M. Brunel, D. Gapais, G.M. Chen, and G.H. Liu, Deformation of leucogranites of the crystalline Main Central Sheet in southern Tibet (China), *J. Struc. Geol., 6*, 535-542, 1984.

Coleman, M.E., and R.R. Parrish, Constraints on Miocene high-

temperature deformation and anatexis within the Greater Himalaya from U-Pb geochronology, *Eos Trans. AGU, 76 (46),Fall Meet. Suppl.*, F708, 1995.

Compston W., I.S. Williams, and C. Meyer, U-Pb geochronology of zircons from Lunar Breccia 73217 using a sensitive, high mass resolution ion microprobe, *J. Geophys. Res., 89*, 8525-8534, 1984.

Copeland, P., T.M. Harrison, W.S.F. Kidd, M. Roden, and Z. Yuquan, Thermal evolution of the Gangdese Batholith, southern Tibet: A history of episodic unroofing, *Tectonics, 14*, 223-236, 1995.

Edwards, M.A., W.S.F. Kidd, and T.M.Harrison, Active medial Miocene detachment in the High Himalaya of the Tibet-Bhutan frontier: A young crystallization age for the Khula Kangri leucogranite pluton, *Eos Trans. AGU, 76 (46)*, Fall Meet. Suppl., F567, 1995.

Foland, K., ^{40}Ar diffusion in homogeneous orthoclase and an interpretation of Ar diffusion in K-feldspars, *Geochim. Cosmochim. Acta, 38*, 151-166, 1974.

Gansser, A., The geodynamic history of the Himalaya, in *Zagros, Hindu Kush, Himalaya–Geodynamic Evolution, Geodyn. Ser., vol 3*, edited by H.K. Gupta and F.M. Delany, AGU, pp. 111-121, Washington, D.C., 1981.

Gansser, A., *The Geology of the Himalayas*, Wiley Interscience, New York, 289 p., 1964.

Grove, M., and T.M. Harrison, ^{40}Ar diffusion in Fe-rich biotite, *Am. Mineral., 81*, 940-951, 1996.

Harrison, T.M., and I. McDougall, The thermal significance of potassium feldspar K-Ar ages inferred from ^{40}Ar/^{39}Ar age spectrum results, *Geochim. Cosmochim. Acta, 46*, 1811-1820, 1982.

Harrison, T.M., I. Duncan, and I. McDougall, Diffusion of ^{40}Ar in biotite: Temperature, pressure and composition effects, *Geochim. Cosmochim. Acta, 49*, 2461-2468, 1985.

Harrison, T.M., O.M. Lovera, and M.T. Heizler, ^{40}Ar/^{39}Ar results for multi-domain samples with varying activation energy, *Geochim. Cosmochim. Acta, 55*, 1435-1448, 1991.

Harrison, T.M., P. Copeland, W.S.F. Kidd, and A. Yin, Raising Tibet, *Science, 255*, 1663-1670, 1992.

Harrison, T.M., P. Copeland, S. Hall, J. Quade, S. Burner, T.P. Ojha, and W.S.F. Kidd, Isotopic preservation of Himalayan/Tibetan uplift, denudation, and climatic histories in two molasse deposits, *J. Geol., 101*, 159-177, 1993.

Harrison, T.M., M.T. Heizler, O.M. Lovera, W. Chen, and M. Grove, A chlorine disinfectant for excess argon released from K-feldspar during step-heating, *Earth Planet. Sci. Lett., 123*, 95-104, 1994.

Harrison, T. M., P. Copeland, W.S.F. Kidd, and O. M. Lovera, Activation of the Nyainqentanghla Shear Zone: implications for uplift of the southern Tibetan Plateau. *Tectonics, 14*, 658-676, 1995a.

Harrison, T.M, K.D. McKeegan, and P. Le Fort, Detection of inherited monazite in the Manaslu leucogranite by ^{208}Pb/^{232}Th ion microprobe dating: Crystallization age and tectonic implications, *Earth Planet. Sci. Lett., 133*, 271-282, 1995b.

Harrison, T.M., F.J. Ryerson, P. Le Fort, A. Yin, O.M. Lovera and E.J. Catlos, A late Miocene-Pliocene origin for the Central Himalayan inverted metamorphism, *Earth Planet. Sci. Lett.*, in press, 1996.

Hauck, M.L., K. D. Nelson, C. Wu, L. D. Brown, W. S. F. Kidd, M. E. Edwards, J. T. Kuo, and W. Zhao, Ramping of the Main Himalayan Thrust and development of the South Tibetan Detachment and Kangmar basement dome: INDEPTH reflection profiles in southern Tibet, *Geol. Soc. Am. Abstr. Programs, 27*, A336, 1995.

Hubbard, M.S., and T.M. Harrison, ^{40}Ar/^{39}Ar age constraints on deformation and metamorphism in the MCT Zone and Tibetan Slab, eastern Nepal Himalaya, *Tectonics, 8*, 865-880, 1989.

Hubbert, M.K., and W.W. Rubey, Role of fluid pressure in mechanics of overthrust faulting, I. Mechanics of fluid-filled, porous solids and application to overthrust faulting, *Geol. Soc. Am. Bull., 70*, 115-166, 1959.

Kidd, W.S.F., P. Yusheng, C. Chengfa, M.P. Coward, J.F. Dewey, A. Gansser, P. Molnar, R.M. Shackelton, and S. Yiyin, Geological mapping of the 1985 Chinese-British (Xizang-Qinghai) Geotraverse route, *Philos. Trans. R. Soc. London, Ser. A, 327*, 287-305, 1988.

Le Fort, P., Himalayas, the collided range. Present knowledge of the continental arc, *Am. J. Sci., 275A*, 1-44, 1975.

Liu, Z.Q., et al., Geologic map of Qinghai-Xizang Plateau and its neighboring regions (in Chinese), scale 1:500,000, Chengdu Inst. of Geol. and Miner. Resour., Acad. Sin., Geol. Publ., Beijing, 1988.

Lovera, O.M., F.M. Richter, and T.M. Harrison, ^{40}Ar/^{39}Ar geothermometry for slowly cooled samples having a distribution of diffusion domain sizes, *J. Geophys. Res., 94*, 17,917-17,935, 1989.

Makovsky, Y., S.L. Klemperer, L. Ratschbacher, J. Mechie, H. Steentoft, R. Meissner, L. Ming, Z. Wenjin, M. Fanle, and G. Jinru, INDEPTH wide-angle profiling in southern Tibet: Mid-crustal reflector truncating the India-Asia suture and magma beneath the Tibetan rift system, *Science*, in press, 1996.

Mattauer, M., Intracontinental subduction, crustal stacking wedge and crust-mantle decollement, in *Collision Tectonics*, edited by M.P. Coward and A.C. Ries, *Geol. Soc. Spec. Publ., 19*, 35-60, 1986.

McDougall, I., and T.M. Harrison, *Geochronology and Thermochronology by the ^{40}Ar/^{39}Ar Method*, 212 pp., Oxford Univ. Press, New York, 1988.

Nieverglet, P., J.-P. Burg, F. Oberli, P. Davy, Z.Z. Diao, and M. Meier, Geology of the Namche Barwa syntaxix (eastern Himalaya): Preliminary report, *in 10th Himalaya-Karakorum-Tibet Workshop Abstract Volume, Mitt. Geol. Inst. der Eidg Tech. Hochsch. Univ. Zürich, 298*, 113 pp., 1995.

Paces, J.B., and J.D. Miller, Precise U-Pb age of Duluth Complex and related mafic intrusions, northeastern Minnesota: Geochronological insights into physical, petrogenetic, paleomagnetic, and tectonomagmatic processes associated with the 1.1 Ga midcontintent rift system, *J. Geophys. Res., 98*, 13,997-14,013, 1993.

Press, W.H., B.P. Flannery, S.A. Peukolsky, and W.T. Vetterling, *Numerical Recipes: The Art of Scientific Computing*, 818 pp., Cambridge Univ. Press, New York, 1988.

Ratschbacher, L., W. Frisch, G. Lui, and C. Chen, Distributed deformation in southern and western Tibet during and after the India-Asia collision, *J. Geophys. Res., 99*, 19,917-19,945, 1994.

Schärer, U., R.-H., Xu, and C.J. Allègre, U-Pb geochronology of Gangdese (Transhimalaya) plutonism in the Lhasa-Xigaze region, Tibet, *Earth Planet. Sci. Lett., 69*, 311-320, 1984.

Schuhmacher, M., E. de Chambost, K.D. McKeegan, T.M. Harrison, and H. Migeon, In situ dating of zircon with the CAMECA ims 1270, in *Secondary Ion Mass Spectrometry SIMS IX*, edited by A. Benninghoven et al., pp. 919-922, John Wiley, New York, 1994.

Turcotte, D.L., and G. Schubert, *Geodynamics: Applications of Continuum Physics to Geological Problems*, 450 pp., John Wiley, New York, 1982.

Wang, X., Z. M. Li, and Qiangba-Xiyiao, Geologic map of the Xigaze-Zedong region, scale 1:100,000, Xizang (Tibet) with report.,568 p., Xizang Bur. of Geol., Lhasa, China, 1983.

Wright, N., P.W. Layer, and D. York, New insights into thermal history from single grain ^{40}Ar/^{39}Ar analysis of biotite, *Earth Planet. Sci. Lett., 104*, 70-79, 1991.

Yin, A., T.M. Harrison, F.J. Ryerson, Chen W., W.S.F. Kidd, and P. Copeland, Tertiary structural evolution of the Gangdese Thrust: southeastern Tibet, *J. Geophys. Res., 99*, 18,175-18,201, 1994.

Zeitler, P.K., Argon diffusion in partially degassed alkali feldspar: Insights from ^{40}Ar/^{39}Ar analysis, *Chem. Geol., 65*, 167-181, 1987.

Zhao, W., K.D. Nelson, and Project INDEPTH Team, Deep seismic reflection evidence for continental underthrusting beneath southern Tibet, *Nature, 366*, 557-559, 1993.

M. Grove, T. M. Harrison, O. M. Lovera, X. Quidelleur, and A. Yin, Department of Earth and Space Sciences, IGPP, University of California, Los Angeles, CA 90024. (e-mail: marty@argon.ess.ucla.edu; tmh@argon.ess.ucla.edu; lovera@argon.ess.ucla.edu)

X. Quidelleur, Institut de Physique du Globe de Paris, Laboratoire de Geochronologie, Université Paris Sud, IPG Paris, 91405 Orsay Cedex, France.

F. J. Ryerson, IGPP, Lawrence Livermore National Laboratory, Livermore, CA 94550. (e-mail: ryerson@s91.es.llnl.gov)

(Received January 8, 1996; revised July 29, 1996; accepted August 7, 1996.)